

MEAN MOTION RESONANCES IN EXOPLANET SYSTEMS: AN INVESTIGATION INTO NODDING BEHAVIOR

Jacob A. Ketchum,¹ Fred C. Adams,^{1,2} and Anthony M. Bloch^{1,3}

¹*Michigan Center for Theoretical Physics
Physics Department, University of Michigan, Ann Arbor, MI 48109*

²*Astronomy Department, University of Michigan, Ann Arbor, MI 48109*

³*Department of Mathematics, University of Michigan, Ann Arbor, MI 48109*

ABSTRACT

Motivated by the large number of extrasolar planetary systems that are near mean motion resonances, this paper explores a related type of dynamical behavior known as “nodding”. Here, the resonance angle of a planetary system executes libration (oscillatory motion) for several cycles, circulates for one or more cycles, and then enters once again into libration. This type of complicated dynamics can affect our interpretation of observed planetary systems that are in or near mean motion resonance. This work shows that planetary systems in (near) mean motion resonance can exhibit nodding behavior, and outlines the portion of parameter space where it occurs. This problem is addressed using both full numerical integrations of the planetary systems and via model equations obtained through expansions of the disturbing function. In the latter approach, we identify the relevant terms that allow for nodding. The two approaches are in agreement, and show that nodding often occurs when a small body is in an external mean motion resonance with a larger planet. As a result, the nodding phenomenon can be important for interpreting observations of transit timing variations, where the existence of smaller bodies is inferred through their effects on larger, observed transiting planets. For example, in actively nodding planetary systems, both the amplitude and frequency of the transit timing variations depend on the observational time window.

Subject headings: planets and satellites: dynamical evolution and stability — planets and satellites: formation — planet-disk interactions

1. Introduction

The current observational sample of extrasolar planets includes many systems with multiple planets, and many systems have orbital period ratios that are close to integer values (e.g., Fabrycky et al. 2012). These systems are thus candidates for being in mean motion resonance (MMR), which represents a special dynamical state for a planetary system. In addition to the necessary period ratio, the other dynamical variables of a resonant system must allow one or more resonance angles (see below for their definitions) to execute oscillatory behavior (e.g., Murray & Dermott 1999; hereafter MD99). One way to describe this requirement is that the resonant angle(s) must reside in a “bound state” within an “effective potential well”. Because of the special conditions required for a planetary system to reside in mean motion resonance, systems found in such states must have a constrained dynamical history. The relative fraction of planetary systems in mean motion resonance thus provides important information regarding planetary formation and early dynamical evolution.

The dynamics of mean motion resonances is often more complex than indicated by standard textbook treatments. This paper explores one such complication called “nodding”, where the resonance angle librates for several cycles and then circulates for one or more cycles before returning to an oscillatory state. This paper addresses the problem using two complementary approaches, i.e., both full numerical integrations of the planetary systems and the construction of model equations obtained through expansions of the disturbing function. The expansion approach produces a large number of terms, and we identify the ones that allow for nodding behavior. These two approaches are in good agreement, and show that nodding often occurs when a small body is in mean motion resonance with a larger planet. The immediate goal of this paper is to obtain a better understanding of nodding in the context of three-body planetary systems. The over-arching goal is to provide a more detailed basis for interpreting observed systems that are found in or near resonance, including systems that exhibit transit timing variations (TTVs), which provide a means of detecting small bodies interacting with larger planets in transit (Agol et al. 2005).

We note that previous dynamical studies, especially concerning asteroids in our Solar System, have found behavior that is qualitatively similar to the nodding phenomenon explored herein. For example, asteroids near the 2:1 MMR with Jupiter are predicted to alternate between two modes of libration (Greenberg & Franklin 1975). In one mode, the longitude of perihelion for the asteroid librates about the longitude of perihelion for Jupiter; in the other mode, the aphelion of the asteroid librates about the longitude of conjunction. The asteroids are predicted to alternate between the two different modes. Similar apocentric resonances are found for the Hildas asteroid group (see Henrard et al. 1986; Ferraz-Mello 1988). The phase space of these dynamical systems contain separatrices for both global and

internal (secondary) resonances (Morbidelli & Moons 1993); chaotic motion near the separatrices can lead to crossing, and hence to alternating modes of libration (see also Michtchenko et al. 2008ab). In addition to appearing in planetary systems, this nodding behavior arises in other dynamical systems, including the driven, inverted pendulum (Acheson 1995). Additionally, nodding systems sometimes exhibit similar phase characteristics to other known dynamical systems, such as the the Duffing oscillator (Guckenheimer & Holmes 1983).

Both nodding and transit timing variations can occur in planetary systems in or near mean motion resonance. Observed resonant and near-resonant systems provide important information about planetary systems. As one example, external perturbations can remove systems from resonance if the perturbations are large enough and if they act over a sufficiently long time (Adams et al. 2008; Rein & Papaloizou 2009; Lecoanet et al. 2009; Ketchum et al. 2011a); furthermore, such conditions can be realized in the circumstellar disks that form planets. As a result, planetary systems that are observed in resonance today must not have been greatly perturbed in the past, or they must have been subsequently influenced by significant dissipative interactions. On the other hand, resonances can also act as a protection mechanism, especially for close and massive planets. Indeed, the current sample of exoplanets includes systems that can only exist because of strong resonant interactions; the GJ876 system provides one such example (see Snellgrove et al. 2001; Beauge & Michtchenko 2003; Kley et al. 2005).

As another example, we note that entry into mean motion resonance is non-trivial: If the orbital elements of a planetary system are selected at random, the chance that the system resides in a mean motion resonance is relatively modest (even when the period ratio is chosen to be near the ratio of small integers). However, systems can evolve into resonance states through the process of convergent migration (e.g., Lee & Peale 2002), where, for instance, the outer planet migrates inward faster than the inner planet, and the two bodies subsequently move inward together. Even in this scenario, survival of the resonance can be compromised by overly rapid migration (Quillen 2006), and/or by turbulent forcing from the disk driving the migration (Lecoanet et al. 2009; Ketchum et al. 2011a).

As one potential application of this work, nodding can affect our interpretation of TTVs (Agol et al. 2005). In this setting, unseen small bodies orbit outside observed transiting planets (usually Hot Jupiters). The smaller bodies affect the orbit of the inner, larger planets and lead to small variations in the timing of the transit events. This phenomenon is potentially a powerful method to detect (infer the presence of) smaller, otherwise unobserved, planets in such systems. Indeed, discoveries of this type have already been reported (e.g., Holman et al. 2010; Cochran et al. 2011), and many more are expected in the near future. However, the timing variations are largest when the smaller planets are in or near mean

motion resonance with the larger planet (e.g., Nesvorný & Morbidelli 2008), and such systems are susceptible to nodding as studied herein. Even without the complication posed by nodding, inferring the system properties from observations is a sensitive process (e.g., Veras et al. 2011). In any case, the results of this work will be useful for future interpretation of systems that exhibit transit timing variations.

This paper is organized as follows. In Section 2, we study the nodding phenomena through numerical integrations of multiple planet systems that are near mean motion resonance. This investigation shows that complex dynamical behavior, including nodding, is often present, and outlines the portion of parameter space where it occurs. For systems that exhibit nodding behavior, we then outline the corresponding effects on transit timing variations. In Section 3, we derive a class of model equations to describe nodding behavior. Here we expand the disturbing function for planetary interactions (e.g., MD99), keep the highest order terms, and identify the relevant terms that lead to nodding. The resulting model equations elucidate the dynamical ingredients required for nodding behavior to take place. We conclude, in Section 4, with a summary of our results, a discussion of their implications, and a brief description of future work.

2. Numerical Study of Nodding

2.1. Full 3-body Numerical Simulations

This paper studies nodding of mean motion resonance angles for planet pairs that are near MMR. For simplicity, most of this work focuses on the 2:1 resonance. The term “nodding” here refers to a tendency to repeat a pattern of bounded libration for several cycles followed by one or more cycles of circulation. For intermediate times, the system exhibits behavior of MMR, but intermittent bouts of circulation may produce a cumulative net circulation of the resonance angle over many libration times. In the context of resonant angle phase trajectories, nodding can be described as motion near a separatrix in the phase space. The phase space for internal resonances contain one separatrix, whereas the phase space for external resonances can contain two distinct separatrices. The qualitative differences occur, in part, due to the existence of asymmetric external resonances, which arise when the orbital eccentricity for the test body becomes sufficiently large (Ferraz-Mello et al. 2003). The existence of asymmetric resonance strongly depends on the mass ratio (see Michtchenko et al 2008b); for example, for $m_2 \ll m_1$, all stable orbits are asymmetric (Beauge 1994).

To carry out the study in this section, we numerically integrate the three-body gravitational forces using a Bulirsch-Stoer integration scheme. In addition to gravity, both general

relativistic corrections and stellar tidal damping are included in force calculations, but the inclusion of these additional forces (which are small) are not necessary to produce the interesting features explored in this work. Our system consists of a star with mass $M_* = 1M_\odot$, a massive planet ($m_p = 1M_{jup}$), and a test body ($m = 10^{-6}M_{jup}$). We chose this particular test mass in order to minimize its influence on the planet’s motion and to obtain the clearest dynamical signature of resonance angle nodding. However, nodding is also present for larger masses for the third body (in Section 2.4 we consider masses as large as $m = 10M_\oplus$). The Jovian planet is placed in orbit with period $T_p = 1$ year, and the test body is placed in orbit with initial period $T = 1/2$ or $T = 2$ years for studies involving internal and external resonances, respectively. We choose a benchmark test body eccentricity of $e = 0.15$, which is motivated by previous work (Ketchum et al. 2011a), and we choose from two values for the planet’s initial orbital eccentricity, $e_p = 0.001$ or $e_p = 0.1$.

To fully describe the initial configuration of the system, the initial orbital angles must be specified. We parameterize this study using the set of angles given by $\Delta\varpi_0$ – the relative alignment between the two orbits – and f_0 – the test body’s true anomaly. Unless noted otherwise, all simulations begin with the planet and test body in conjunction. In an attempt to sample the available resonance angle phase space resulting from a choice of initial orbital elements $\{e_p, e, \alpha, \Delta\varpi\}$, values of f_0 spanning the full range $-\pi$ to π in increments of $\pi/100$ are sampled. Following this systematic approach, those states that have phase trajectories occurring near a separatrix, which ultimately lead to nodding, are easily found.

The simulations are integrated for 10^4 years, a sufficient amount of time to capture several secular cycles for most initial configurations (for completeness, note that the parameter space for external resonances contain small regions where the secular cycle’s period is infinite – see Michtchenko et al. 2008b). The energy for a typical system that experiences no significant close encounters is conserved to better than one part in 10^{10} . The planets’ period ratio is monitored to confirm that the system remains nearly integer commensurate during the integration and hence that near resonance has not been compromised by a chance close encounter. The osculating elements for both bodies are recorded once per orbit of the inner planet. Since the libration timescales are of order $\sim 30 - 100$ orbits (albeit with large variations), this sampling cadence is frequent enough to resolve the behavior of the resonance angles. For 2:1 resonances, the resonance angles of interest are

$$\phi = 2\lambda_p - \lambda - \varpi , \tag{1}$$

for a test body internal to the planet’s orbit, and

$$\phi = 2\lambda - \lambda_p - \varpi , \tag{2}$$

for a test body external to the planet’s orbit, where λ is the mean longitude and subscript p denotes the orbital elements belonging to the Jovian planet. And finally, the time rate

of change for the resonance angle, $\dot{\phi}$, is determined by quadratic interpolation, and used to construct resonance angle phase trajectories.

2.2. Nodding Features for Near-Resonance

The range of dynamical behaviors encountered in (or near) mean motion resonance is surprisingly rich (e.g., Michtchenko et al. 2008ab). Presented here is a small representative sample set of the simulations outlined above which display the main features found in these resonance states.

We first consider systems where nodding does *not* occur (see Figure 1). The figure features a system with a configuration and behavior deviating only slightly from the pendulum model of MD99. For this system, the perturbing planet is placed in orbit with semi-major axis $a_p = 1\text{AU}$ and eccentricity $e_p = 10^{-3}$ around a $1M_\odot$ star. A test particle of mass $m = 10^{-6}M_{jup}$ is set in a coplanar orbit with semi-major axis $a = 0.63\text{ AU}$ and orbital eccentricity $e = 0.15$, which places the two orbiting bodies near a 2:1 period ratio. The orbits are initially anti-aligned ($\Delta\varpi_0 = \pi$) and the orbiting bodies placed in conjunction with the test particle near periapse – the system is prepared such that the planet’s influence on the test body’s motion is initially minimized, i.e., the two orbiting bodies cannot be separated further from one another during conjunction given this set of orbital elements. The top panel of Figure 1 shows the resonance angle, ϕ , from equation (1) in blue and the angle of apsides, $\Delta\varpi$, in red. The resonance angle librates with a small amplitude of $\Delta\phi \simeq 0.1$ radians around the equilibrium $\phi = 0$, while the apsidal angle circulates due to a prograde motion of the test particle’s longitude of periastron – the planet’s longitude of periastron, ϖ_p , does not move significantly. In the limit of small orbital eccentricities e and e_p , the test body’s true anomaly approximately coincides with the resonance angle at instances of conjunction. Thus, for this system, these dynamics depend mainly upon our choice for $|f_0|$ and are independent of our choice for $\Delta\varpi$. The bottom panel of Figure 1 shows the phase trajectory for the resonance angle. This panel depicts a phase trajectory analogous to small oscillations of a simple pendulum, as expected. In this respect, the pendulum model of the circular restricted three body problem provides a sufficient model for resonances arising from orbital configurations of this type – although the planet’s orbital eccentricity is non-zero, dynamical deviations from the pendulum model of the circular restricted three body problem incurred through small departures from circular symmetry are negligible.

As $|f_0|$ increases from 0 to π , the amplitude of oscillations also increase until the conjunction line approaches apoapse, where the system reaches a separatrix and the resonance angle will circulate rather than oscillate. Figure 2 shows a system identical to that of Fig-

ure 1 in all aspects except that $f_0 \approx 2\pi/3$ radians, so that the resonance angle exhibits larger oscillations. The libration frequencies of the two systems however, are practically identical with frequency $\omega \sim 0.03 \text{ yr}^{-1}$.

For external resonance scenarios, the behavior is significantly different. Figure 3 shows the first example of nodding. In the figure, $|f_0| \sim \pi$ so initial conjunction is close to apastron of the test body’s orbit, and the orbits are initially anti-aligned, $\Delta\varpi_0 = \pi$. This set of initial orbital elements gives the maximum possible spatial separation between the planet and test body. The resonance angle ϕ , given by equation (2) and shown in blue in the top panel of the figure, seems to be attracted to one of two stable fixed points, with an unstable fixed point effectively located at $\phi = \pi$. This is an example of an asymmetric resonance (Lee 2004; compare with Callegari et al. 2004), and the existence of the two equilibrium points on either side of $\phi = \pi$ are due to a bifurcation occurring in the dynamics for sufficiently large test body orbital eccentricity (e.g., Michtchenko et al. 2008b). In this case, the system was configured near a different kind of separatrix than those encountered for internal resonances, and motion near this separatrix leads to nodding behavior that is unique to the external case. In general, the planar three-body problem has two degrees of freedom, with two proper frequencies: resonant and secular ones. As a result, oscillations of the problem (including nodding) must be combinations of the two proper frequencies.

Note that there are several secular cycles shown in Figure 3, and during each secular cycle the resonance angle seems to choose one of three different libration modes – (a) resonance oscillations enclosing some point to the left of $\phi = \pi$, (b) oscillations enclosing some point to the right of $\phi = \pi$, or (c) oscillations enclosing all three points. As $|f_0| \rightarrow 0$ for similarly prepared systems, resonant oscillation amplitudes reach the maximum possible value $\Delta\phi \approx \pi$ radians before circulating. Encountered here is another separatrix, which is analogous to the separatrix for the internal resonance. In contrast to the internal resonance separatrix, the phase space trajectory for large amplitude oscillations here takes a different shape – the resonant angle’s speed decreases (increases) as it approaches (departs from) the test body’s apoapse location. Systems on such phase trajectories appear to nod once per one resonant libration, as depicted in Figure 4 where $f_0 \approx \pi/4$. In this regard, the resonance angle moves as if it lives in a quartic potential, with a local maximum at $\phi = \pi$, two minima near $\phi = \pi/2$ and $\phi = 3\pi/2$, and a maximum at $\phi = 0$. This feature of the motion near the outer separatrix of an asymmetric outer resonance can lead to a period increase or decrease by a factor of two for transit timing variations, a result presented later on in this paper.

The nodding features become more prevalent as the perturber’s eccentricity increases, where the resonance angle can begin accumulating a net circulation over longer times. Figures 5 and 6 provide examples of the type of circulation behavior we observe in simulations.

These two figures also showcase the stark contrasts between nodding for internal and external resonances, respectively. In this comparison, the planet’s orbital eccentricity is $e_p = 0.1$ – substantial enough to be well outside the *circular* restricted three body regime (where the pendulum model is strictly valid). Both examples show the tendency for $\Delta\varpi$ to circulate, on average, with a periodic component resulting from secular interactions, and, on average, the resonance angle circulates at the same rate. For times shorter than secular timescales, however, the resonance angle librates with some amplitude, not exceeding $\Delta\phi = \pi$, around some equilibrium point. The point about which the resonance angle oscillates differs between the external and internal perturber cases. For the pendulum model of the circular restricted 3-body problem, the equilibrium point is located at $\phi = 0$ for internal resonances, while for external resonances it is $\phi = \pi$. We stress, however, that the pendulum model is an over-simplification for the regime under consideration.

Figure 5 shows the eccentricities (top panel), resonance angle (middle panel), and phase trajectory (bottom panel) for a system the same set of initial orbital elements as was used in Figure 1, with the exception that here the planet’s orbital eccentricity $e_p = 0.1$. The system is prepared with anti-aligned orbits and the orbiting bodies in conjunction near the test body’s apoapse. Recall from the above discussion that this particular configuration places the resonance angle near a separatrix in its phase space. The figure shows slightly more than 3 complete secular cycles, each lasting ≈ 3300 yrs, which corresponds to hundreds of libration times. During each secular cycle, the test body’s orbital eccentricity (shown in black in the top panel) increases from its initial value of $e = 0.15$ up to $e \sim 0.6$ (where the two orbits intersect for a time), and then decreases close to its initial value. For times that are shorter than secular timescales and longer than libration timescales, the resonance angle undergoes large amplitude oscillation about the test body’s periapse. In the previous case, when the planet’s orbit was nearly circular, the motion of the test body’s apsidal angle was steady circulation. In the present case where the Jovian planet’s eccentricity is substantially larger, the azimuthal symmetry of the star-planet Keplerian system has been sufficiently broken and the evolution of the test body’s osculating elements depends sensitively upon the orbital alignment (given by the apsidal angle, $\Delta\varpi$). The red curve in the middle panel of Figure 5 shows the apsidal angle, which, over the course of one secular cycle, oscillates once very slowly about $\Delta\varpi = \pi$, then very abruptly passes $\Delta\varpi = 0$ in the retrograde direction. Generally, as the apsidal angle approaches $\Delta\varpi = \pi$ (i.e., as the orbits approach anti-alignment), the test body’s eccentricity decreases, and as the orbits rotate out of anti-alignment, the eccentricity increases. As the apsidal angle approaches $\Delta\varpi = 0$, the orbits come into alignment, and with comparatively large orbital eccentricities, the planet exerts greater influence on the motion of the test body than in cases where it’s orbit is nearly circular (see Batygin & Morbidelli 2011 for a detailed analysis of secular dynamics). As a consequence, the resonance angle circulates

once or twice until the orbits rotate out of alignment, and the system enters into yet another secular cycle that deviates only slightly from the one just described. The test body can exhibit a wide range of eccentricity growth/decay during a secular cycle, and the duration of the secular cycle depends on the details of the initial 3-body configuration. However, the generic behavior of the osculating orbital elements described above during a secular cycle for any choice of $\Delta\varpi_0$ is robust. As long as the orbiting bodies are in conjunction with f_0 for the test body near apoapse, the resonance will reside near the separatrix in phase space and the system can experience nodding for states near mean motion resonance.

For the external resonance shown in Figure 6, the system is initially configured with anti-aligned orbits $\Delta\varpi = \pi$ and conjunction occurring near the test body’s apastron $f_0 \simeq \pi$. The test body’s orbital eccentricity is sufficiently large to place the system near an asymmetric resonance, meaning there are generally two libration points. The exact locations of the libration points depend on the instantaneous orbital eccentricity (shown by the black curve in the top panel of the figure), but for ease of discussion, we take them to be $\approx \pi \pm \pi/2$. During a secular cycle, the resonance angle ϕ oscillates with an amplitude $\pi/4 \lesssim \Delta\phi < \pi/2$. There are 6 full secular cycles shown here, each lasting ~ 1600 years. The test body’s periapse circulates in the retrograde direction on average, so the apsidal angle $\Delta\varpi$ circulates. The nodding cycle, eccentricity growth/decay, and the apsidal angle circulation are all governed by the secular cycle and coordinate together to produce the specific nodding behavior of the resonance angle. As the two orbits’ major axes rotate to become more perpendicular, the test body’s eccentricity grows, and resonant oscillation amplitudes decrease, resulting in a tightening of libration. As the two orbits rotate so that their major axes become parallel (orbits either aligned or anti-aligned), the test body’s orbital eccentricity decreases. The eccentricity attains a minimum value when the major axes are in alignment, reaching its smallest values when the orbits’ periapses become aligned (as opposed to anti-aligned). As the test body’s orbital eccentricity decreases, the libration points of the asymmetric resonance move closer to π and the resonant angle’s oscillation amplitudes generally increase, which in turn moves the phase trajectory toward one of the two separatrices. With the orbits near alignment ($\Delta\varpi \approx 0$), the phase trajectory approaches the outer separatrix, and circulation becomes possible. When the orbits are nearly anti-aligned, the phase trajectory approaches the inner separatrix, which separates bounded libration around a single stable point from libration around both. Here, it is possible for the phase trajectory to jump across π to the adjacent stable point. The number of times the resonant angle circulates or jumps back and forth between stable points during major axes alignment varies from secular cycle to cycle. However, the nodding cycles tend to mimic preceding cycles, and every so often abrupt changes will occur which again persist over multiple nodding cycles, until another abrupt change occurs. This behavior then repeats.

To summarize, we have studied both internal and external resonance scenarios using both nearly circular planet orbits ($e_p = 10^{-3}$) and an orbit that departs from circular ($e_p = 0.1$). We took a benchmark value for the test body’s initial orbital eccentricity of $e = 0.15$, but this value varied with the secular cycle, reaching values as high as $e \simeq 0.6$ and as low as $e \simeq 0.01$. Variations to the test body’s orbital eccentricity increased in simulations which included larger planet eccentricity. On secular timescales, the 2:1 resonance angle may exhibit bouts of circulation with regular libration in between circulation events (the phenomenon we call nodding). Nodding is common when the planet’s orbital eccentricity is sufficiently large, where we find an approximate threshold of $\sim e_p \gtrsim$ a few $\times 10^{-2}$. Nodding systems with larger orbital eccentricities are able to obtain greater net circulation than systems where both orbital eccentricities are small. However, the relative orbital alignment and the test body’s true anomaly at the moment of conjunction affect both the period of the nodding cycle and the libration width during intermediate times. Both internal and external resonances exhibit nodding, but prominent qualitative differences in the nodding signatures between the two configurations exist. Because of our choice of initial test body orbital eccentricity, asymmetric resonances are found for external cases, where libration occurs around points $\phi = (1 \pm \delta/2)\pi$ with $\delta \approx 1$ for $e_0 \approx 0.15$ (e.g., Lee 2004; cf. Callegari et al. 2004). Consequently, for external resonances, libration amplitudes are typically smaller ($\Delta\phi \lesssim \pi/4$) for large e_p . For nearly circular planet orbits, large amplitudes ($\Delta\phi \lesssim \pi$) may persist for external resonances, and appear to librate about $\phi = \pi$. However, the resonance angle’s motion slows as it passes $\phi = \pi$, which is distinctively different from large amplitude oscillations for the internal resonance case.

2.3. Dynamical Map of Nodding in the Hot Jupiter Problem

In this section we explore the nodding phenomenon for Hot Jupiters. Because of the existence of the asymmetric resonance and the additional separatrix that comes along with it, the external resonance is particularly interesting in the context of the Hot Jupiter problem (where smaller bodies could be found in outer orbits – see Ketchum et al. 2011b). For completeness, we explore how the resonance angles of the external 2:1 near resonance are affected by the external test body’s orbital eccentricity and by the orbital alignment between the planet and the test body. To perform this study, we use typical parameters of Hot Jupiter systems, where a Jovian planet (with mass $m_p = 1M_{jup}$, orbital eccentricity $e_p = 0.04$, and orbital period $T_p = 4$ days) orbits a $1M_\odot$ star with a small planet (with mass $m = 1M_\oplus$ and orbital period $T = 8$ days) orbiting external to the Star-Jovian system. We take orbital eccentricity values for the test body between $-3 \leq \log_{10} e \leq -1/3$ in equally spaced logarithmic increments. For each value of the test body’s eccentricity, we perform an

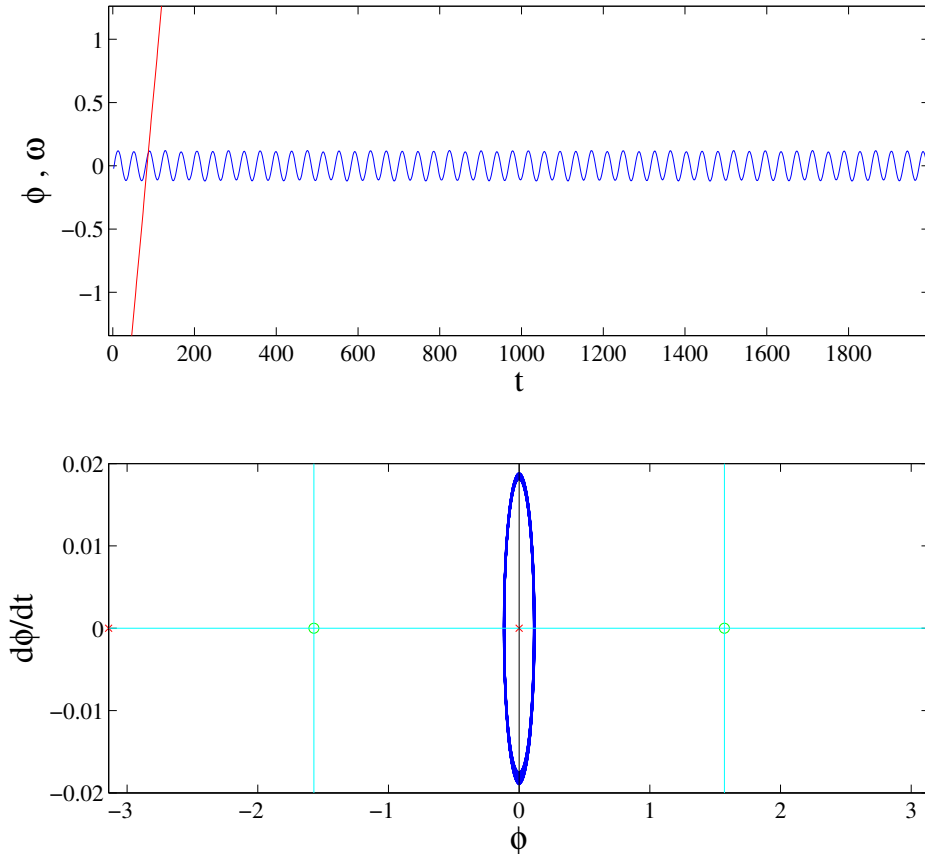


Fig. 1.— Internal 2:1 near-resonance with periaapses initially anti-aligned ($\Delta\varpi = \pi$), test body near periastron at conjunction ($f_0 \approx 0$), and $e_p = 10^{-3}$. All angles are in radians and time is in years. The *top panel* shows the resonance angle, ϕ (blue curve), and the angle of apsides, $\Delta\varpi$ (red curve). In this example, resonance angle nodding does *not* occur. The *bottom panel* shows the phase trajectory of the resonance angle during the full 10^4 years of simulation. This system is close to the text book example of mean motion resonance described by the pendulum model (see Murray & Dermott 1999). The libration amplitude is small ($\Delta\phi \sim 0.1$ rad) and the equilibrium point for oscillations is at $\phi = 0$.

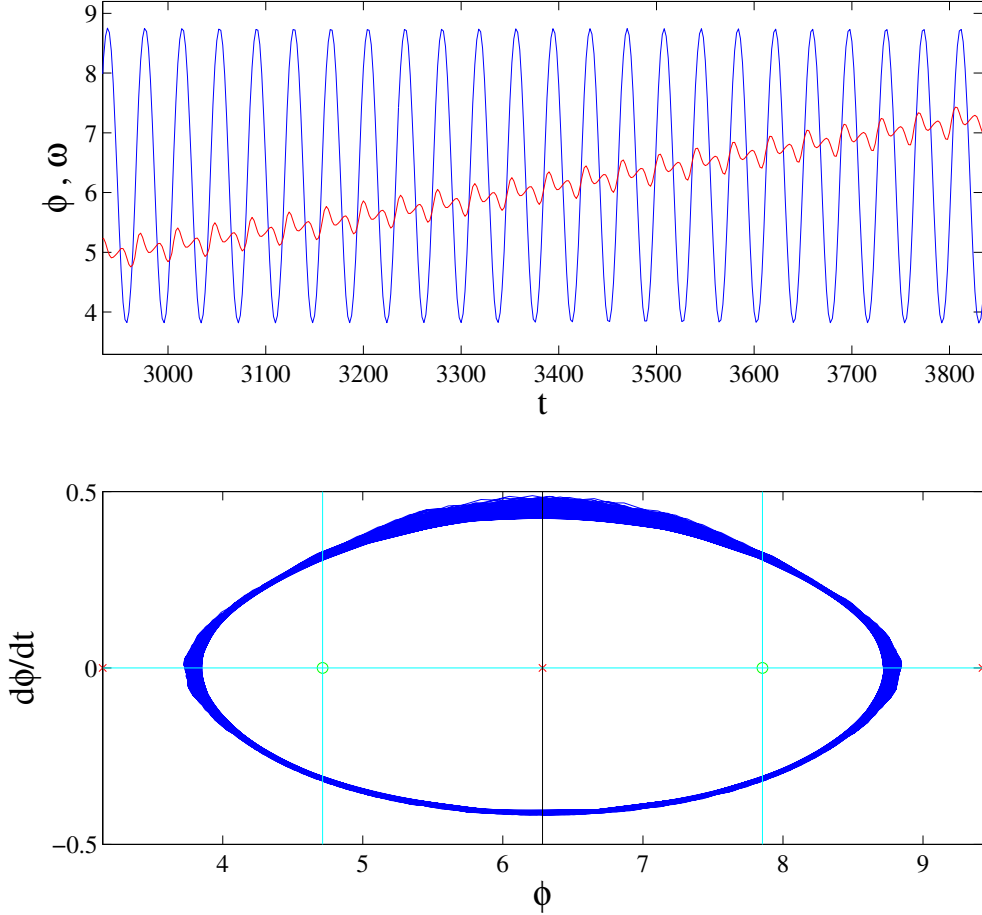


Fig. 2.— Internal 2:1 near-resonance with periaapses initially anti-aligned ($\Delta\varpi = \pi$), test body closer to apastron than to periastron during initial conjunction with a true anomaly $f_0 \approx 2\pi/3$, and the perturbing planet’s orbit nearly circular with an eccentricity of $e_p = 10^{-3}$. All angles are in radians and time is in years. The *top panel* depicts the resonance angle (blue curve) and the angle of apsides (red curve). The resonance angle undergoes large amplitude oscillations of $\Delta\phi \geq 3\pi/4$ due to the test body’s large angular displacement from periastron of its orbit during the initial conjunction with the perturbing planet. In this example, resonance angle nodding does *not* occur. The *bottom panel* shows the phase trajectory for the resonance angle over the full 10^4 years of the simulation, which oscillates about 0 (modulo 2π) and doesn’t circulate at anytime.

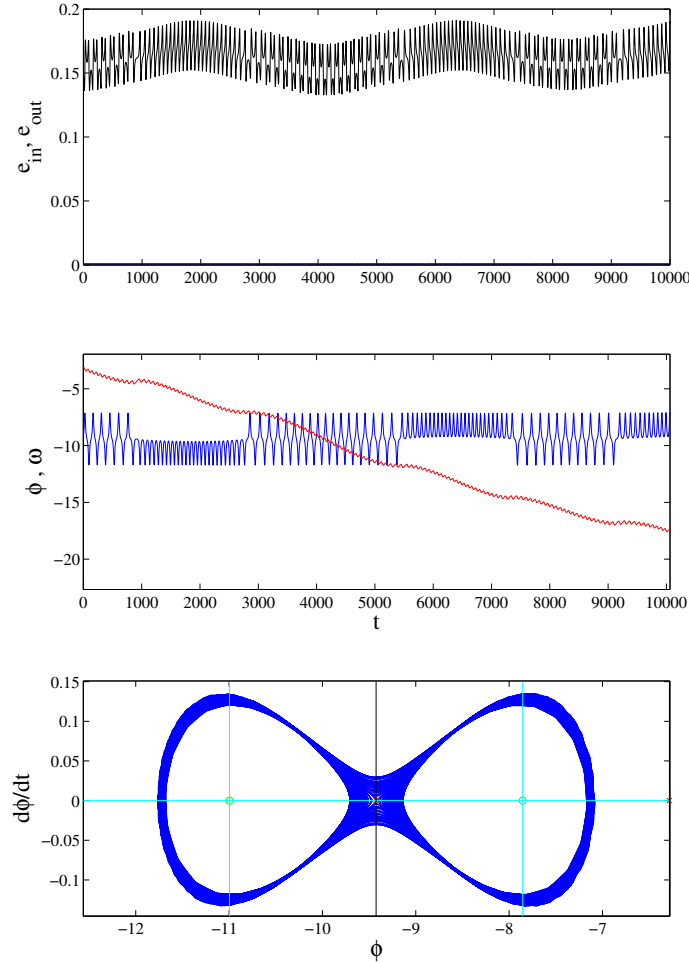


Fig. 3.— External 2:1 near-resonance with periapses initially anti-aligned ($\Delta\varpi \approx \pi$), test body near apastron at conjunction ($f_0 \approx \pi$), and a nearly circular planetary orbit with eccentricity $e_p = 10^{-3}$. All angles are in radians and time is in years. The *top panel* shows the time series of the test body’s eccentricity (black curve – taking values between $0.14 \lesssim e \lesssim 0.18$) and the planet’s eccentricity (blue curve – nearly constant at $e_p \simeq 10^{-3}$). The *middle panel* shows the resonance angle, ϕ (blue curve), and the angle of apsides, $\Delta\varpi$ (red curve). The resonance angle jumps between two points of attraction located near $\pi/2$ and $3\pi/2$ (mod 2π) – sometimes librating around one of these two points many times (e.g., for times between $1000 \lesssim t \lesssim 3000$) before jumping to the opposite point of attraction – this is one form of nodding. The *bottom panel* shows the resonance angle’s phase trajectory for the entire 10^4 years of simulation. This trajectory traces out a complex dance around the inner separatrix of the phase space of the external 2:1 asymmetric resonance.

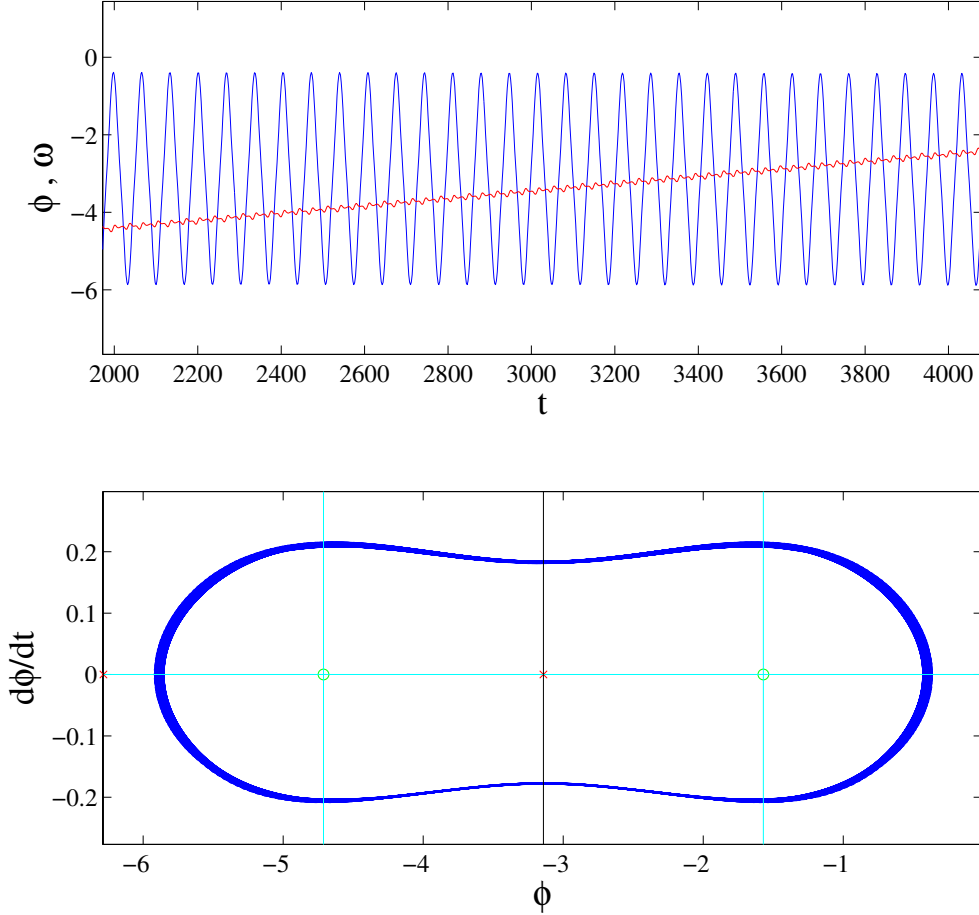


Fig. 4.— External 2:1 near-resonance with periaapses initially anti-aligned ($\Delta\varpi \approx \pi$), test body displaced $\approx 40^\circ$ from periastron at conjunction ($f_0 \approx \pi/4$), and a nearly circular planetary orbit with eccentricity $e_p = 10^{-3}$. All angles are in radians and time is in years. The *top panel* shows the resonance angle, ϕ (blue curve), and the angle of apsides, $\Delta\varpi$ (red curve). The resonance angle repeatedly jumps between two points of attraction located near $\pi/2$ and $3\pi/2$ (mod 2π) – this behavior is one form of nodding. The *bottom panel* shows the resonance angle’s phase trajectory for the entire 10^4 years of simulation. The resonance angle’s motion temporarily slows as it passes apoastron of the test body’s orbit $\phi \approx -\pi$, and accelerates producing sharper peaks in the resonance angle signal of the top panel, in contrast to the internal resonance case (compare with Figure 2).

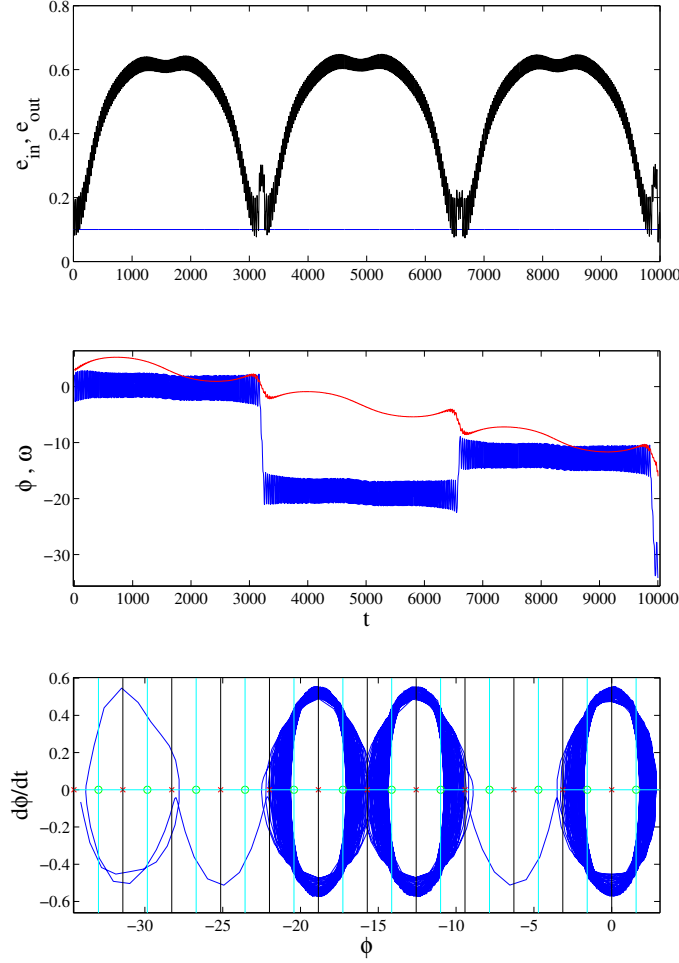


Fig. 5.— Internal 2:1 near-resonance, periapses initially aligned ($\Delta\varpi \approx 0$), test body near apastron during initial conjunction ($f_0 \approx \pi$), and the external planet’s orbit with eccentricity is $e_p = 0.1$. All angles are in radians and time is in years. The *top panel* shows the eccentricity time series for both the test particle (black curve) and the planet (blue curve). The test body’s eccentricity reaches values in excess of $e \gtrsim 0.6$ and as low as $e \lesssim 0.1$, the planet’s orbital eccentricity does not vary significantly. The *middle panel* shows the time series for the resonance angle (in blue) and $\Delta\varpi$ (in red). The resonance angle librates about $\phi \approx 0$ with a varying amplitude $\pi/2 \lesssim \Delta\phi \lesssim \pi$ for large stretches of time, and suddenly circulates once (at time close to $t \approx 6500$ years) or twice (at time $t \approx 3000$ years). This is a form of nodding. The moments in time where the nodding events occur are correlated with the times that the test body’s orbital eccentricity is comparable to the planet’s orbital eccentricity, $e \simeq e_p$, and to times when the orbits are aligned (the angle of apsides $\Delta\varpi \approx 0$ modulo 2π). The *bottom panel* shows the corresponding phase trajectory of the resonance angle, $\dot{\phi}$ vs ϕ .

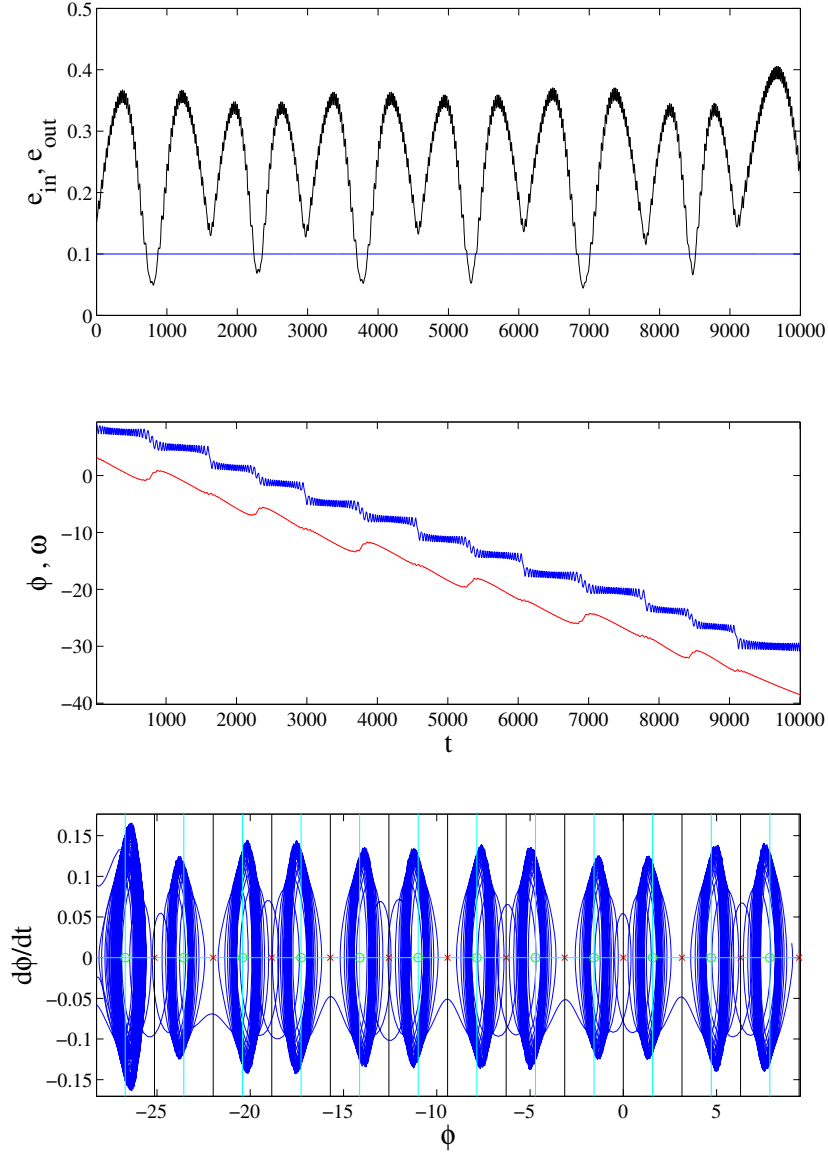


Fig. 6.— External 2:1 near-resonance, periapses anti-aligned ($\Delta\varpi \approx \pi$), test body near apoastron during initial conjunction ($f_0 \approx \pi$), and planet on an eccentric orbit with $e_p = 0.1$. All angles are in radians and time is in years. The *top panel* shows the eccentricity time series for both the test particle (black curve) and the perturber (blue curve). The planet’s eccentricity remains nearly constant during the simulation, while the test body’s eccentricity reaches values up to $e \approx 0.4$ and down to $e \approx 0.05$. The *middle panel* shows the time series for the resonance angle (in blue) and $\Delta\varpi$ (in red). The *bottom panel* shows the phase trajectories of the resonance angle, $\dot{\phi}$ vs ϕ .

ensemble of 200 similarly prepared systems, each with a slightly different initial apsidal angle between $-\pi < \Delta\varpi \leq \pi$ in equally spaced increments. Both the Hot Jupiter and the smaller rocky planet begin each simulation located at the periastron of their respective orbits (not necessarily in conjunction with one another). The parameter space outlined by the above conditions contains 28,560 points, each of which are integrated for up to 200,000 orbits of the Jovian planet (≈ 2000 years). During each individual simulation, we keep track of the displacement of both the resonance angle ϕ and the angle of apsides $\Delta\varpi$, as well as the total number of times the resonance angle passes the test body’s periastron (the latter provides a rough measure of the number of circulation events that take place during the simulation).

The results of the survey are shown as a dynamical map in Figure 7. Each pixel in the figure is composed of an admixture of the three colors red, green, and blue. The amount of each color within a given pixel represents different behavioral characteristics of the angles of interest: *(i)* Red measures the resonance angle’s final angular displacement, *(ii)* Green measures the angle of apsides final angular displacement, and *(iii)* Blue measures the resonance angle’s final angular displacement in comparison to the total number of circulation occurrences during the given simulation. We use the ensemble averages for each category to gauge the overall shade of each color of the survey.

Admittedly, our metric for defining each color’s particular shade in each pixel is somewhat arbitrary, so we refrain from providing specific details about it here. However, in general our metric produces a bright color for smaller deviations from the initial state in comparison to the ensemble’s average deviation, and a darker shade corresponds to a larger deviation than average. We provide a brief interpretation of the prevalent color combinations presented in the figure as follows: *RED*: ϕ strictly librates (no circulation events) and $\Delta\varpi$ circulates; *YELLOW*: Both ϕ and $\Delta\varpi$ librate (minimal circulation); *GREEN*: $\Delta\varpi$ librates, but ϕ circulates quickly; *PURPLE*: ϕ circulation events encountered, but direction of circulation is erratic, and $\Delta\varpi$ circulates; *CYAN*: relatively few circulation events for both ϕ and $\Delta\varpi$ and direction of circulation is consistent; *BLACK*: both ϕ and $\Delta\varpi$ circulate rapidly; *BLANK*: either *(i)* premature termination of the simulation due to a scattering or collision event for the test body, or *(ii)* a period ratio between the planet and test body that deviates by more than 10% once the simulation reaches its time limit.

Although the details appearing in the Figure 7 are intricate and rich, there two main features that we want to emphasize here. [1] The existence of the large, red islands appearing near $(\log(e), \Delta\varpi_0) = (-0.5, \pi/2)$ and the absence of the red islands for values $\log(e) \lesssim -1$ is in agreement with previous findings that for $m_2 \ll m_1$, stable oscillations orbits are asymmetric (Beauge 1994). These large red islands are regions of parameter space where the resonance angle does not circulate at any point in time during the 200,000 orbit

simulation. [2] The diagram shows an apparent pitchfork bifurcation occupying this mapping. For low test body eccentricities, rapid circulation occurs for initial apsidal angles, indicated by the thin horizontal tracks of dark (almost black) pixels located around $\Delta\varpi = \pm\pi/2$. (For completeness, note that the secular angle is not defined in the limit $e \rightarrow 0$; here the eccentricity axis is presented on a logarithmic scale so that $e > 0.001$.) As the eccentricity is increased, these tracks converge to a single horizontal line at the center of the map, where at $e \approx 0.1$ rapid circulation of both ϕ and $\Delta\varpi$ occurs for initial apsidal angle $\Delta\varpi \approx 0$. This trend in the dynamics of the resonance angles, as the exterior test body's eccentricity is increased, is consistent with past studies (e.g., Lee 2004) and, perhaps, reveals further details about the onset of the asymmetric exterior 2:1 resonance.

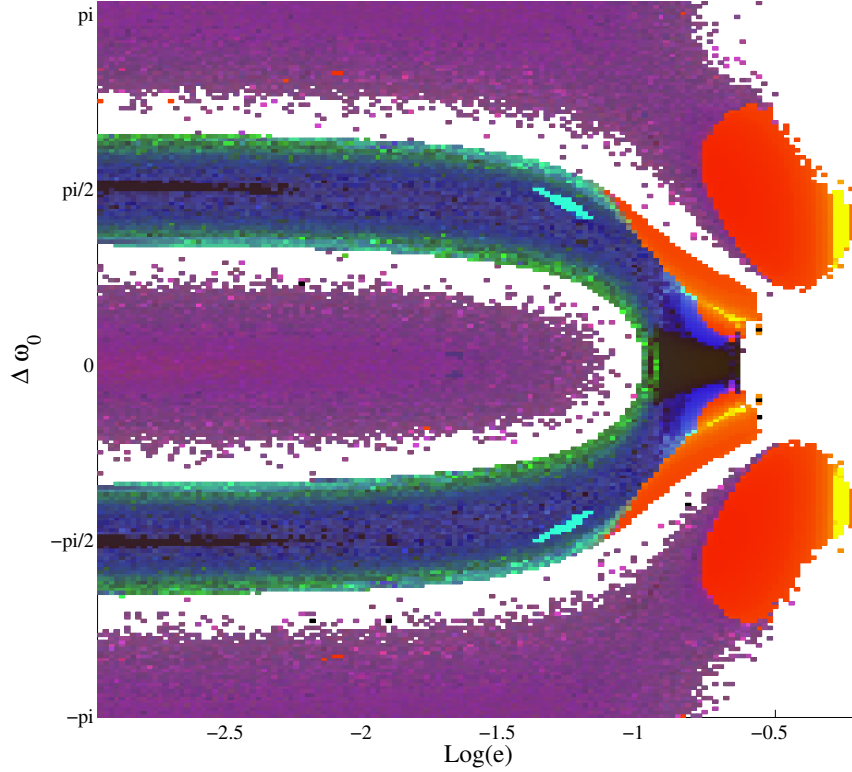


Fig. 7.— Dynamical map of the resonance and apsidal angles’ relative amounts of accumulated circulation during simulations lasting 200,000 orbits (≈ 2000 years) for the external 2:1 near-resonance. All angles are given in radians. Each pixel in this figure represents one simulation with a given initial apsidal angle, $\Delta\varpi$ (vertical axis), and test body orbital eccentricity, $\log_{10} e$ (horizontal axis). This figure is a mosaic of 28,560 different simulations performed as described in the text. Each pixel is colored with an admixture of red, green, and blue. The particular shade of each color signifies the relative amount of circulation, hence nodding, using three different metrics – see text for full description. This set of simulations was performed under the context of a Hot Jupiter scenario, i.e., the planet has eccentricity $e_p = 0.04$, mass $m_p = 1 M_{jup}$, and period $T_p = 4$ days, and the test body has mass $m \approx 1M_{\oplus}$ and period $T = 8$ days, both orbiting a $1M_{\odot}$ star. Each simulation begins with the planet and test body located at periastron of their respective orbits. This figure shows what looks like a pitchfork bifurcation in this parameter space (perhaps due to the transition from symmetric to asymmetric resonances following from left to right across map). For low test body eccentricities, rapid circulation occurs for initial apsidal angles $\Delta\varpi = \pm\pi/2$, and as the initial eccentricity increases, these tracks converge in the center, where, at $e \approx 0.1$, rapid circulation occurs for states with an initial apsidal angle $\Delta\varpi \approx 0$.

2.4. Transit Timing Variations in the Presence of Nodding

One potential channel for discovering terrestrial sized exoplanets involves observing variations in the transit times for a Hot Jupiter (e.g., Agol et al. 2005). These transit timing variations (TTVs) will be largest if the body responsible for the variations is in (or near) a mean motion resonance with the Hot Jupiter. Of the multiple-planet systems known to date, many of the adjacent planet pairs have period ratios that are close to small integer ratios, with 2:1, 3:2, and 3:1 being the most populated, in order of decreasing frequency (e.g., Fabrycky et al. 2012). These observations suggest that a planet, whose presence produces transit timing variations of a transiting Hot Jupiter, is more likely to be near MMR, not deep in MMR with the Hot Jupiter. On the other hand, planet-pairs could still be deep in resonance while the ratio of their orbital periods deviates from exact resonance by as much as 20% (e.g., Batygin & Morbidelli 2012). As shown in the previous section, planetary systems near MMR can exhibit distinctive and interesting behavior — nodding of the resonance angle. This phenomenon can lead to interesting signatures in TTVs, which are considered in this section.

As outlined above, in order for nodding to arise, the larger planet must have nonzero eccentricity. However, Hot Jupiters are subject to tidal forces, which act to circularize their orbits. On the other hand, the observed orbits of Hot Jupiters are often eccentric: The current sample includes 242 planets with semimajor axes $a < 0.1$ AU (Exoplanets Data Explorer 2012) and 79 of these planets have orbital eccentricity in the range $0.02 < e < 0.6$ (and 41 orbits have $e > 0.10$). Some fraction of the Hot Jupiters are thus expected to undergo nodding (if smaller companion planets are also present).

The Hot Jupiters could have nonzero eccentricity for several reasons: [1] The tidal circularization time for 4-day orbits is typically $\tau_{circ} \sim 1$ Gyr (Goldreich & Soter 1963; Hut 1981), and observed systems have ages of 2 – 5 Gyr. As a result, the initial eccentricity is decreased by a factor of “only” $\sim 7 - 150$. If, for example, the starting eccentricity $e_0 = 0.30$, the observed eccentricity $e \approx 0.002 - 0.04$; younger systems with higher starting eccentricities can have even larger values. [2] The tidal circularization time grows with a high power of semimajor axis, $\tau_{circ} \sim a^{13/2}$ (Hut 1981), so that planets with slightly larger orbits have much longer circularization times and hence larger eccentricities. [3] The time required for tidal circularization depends on the tidal quality factor Q (Goldreich & Soter 1963), which depends on the internal structure of the planet. Since observed planets are inferred to have a wide range of structures for a given mass (e.g., Bodenheimer et al. 2003), we expect a wide range of Q values. [4] In multiple planet systems, massive distant planets can drive Hot Jupiters to have nonzero eccentricities (Adams & Laughlin 2006).

To demonstrate the possible effects of nodding on transit timing variations of a Hot

Jupiter, we perform additional simulations. We place two planets in orbit around a $1M_{\odot}$ star – a $1M_{jup}$ planet in a 4 day orbit and a $1M_{\oplus}$ planet in an 8 day orbit. The periastra are approximately anti-aligned $\Delta\varpi \approx \pi$, and the planets are initially placed near conjunction with the Hot Jupiter at periastron. The orbits are set to be coplanar. The initial eccentricity of the smaller planet is taken to be $e = 0.15$, whereas the eccentricity of the Hot Jupiter has values $e_p = 0.1$ and $e_p = 0.01$. For each choice of e_p , we then performed numerical integrations using the integration scheme described above and recorded the times that the center-to-center displacement between the star and Hot Jupiter were parallel to some arbitrary line of sight. Neither light travel time nor transit duration variations are corrected for during the simulations – a more rigorous study should take into account the light travel time from the star to the Hot Jupiter, and should consider the surface-to-surface grazing chord between the star and Hot Jupiter as the line-of-sight rather than the center-to-center line (Veras et al. 2011). However, these are higher order corrections and are not considered here.

Figure 8 shows the results of one such simulation for the larger eccentricity $e_p = 0.10$ of the Hot Jupiter. The resonance angle, shown in blue on the top panel, begins in one mode of oscillation, is caught in libration while being passed back and forth between fixed points near $-\pi/2$ and $-3\pi/2$, and then settles on the $-3\pi/2$ fixed point for nearly 20 librations. At $t = 10$ years (≈ 1000 orbits), the periastra have rotated into near alignment $\Delta\varpi \approx 0$, and the resonance angle undergoes a different type of nodding than exhibited at the beginning, a mode which is characterized by free circulation across the unstable point located at $\phi = -2\pi$. Near the $t = 12$ year mark, the resonance angle enters into a mode of libration around a single fixed libration point at $\phi \simeq -5\pi/2$. This libration undergoes around 20 oscillations, at which time the cycle starts over from the beginning and is repeated several times. The particular cycle illustrated here, which produces the nodding pattern, is similar to that exhibited by the system represented in Figure 6; the initial orbital configurations are nearly identical. However, the mass of the smaller body for this case, with $m = 1M_{\oplus}$, is much larger and the two planets are located much deeper inside the stellar potential than in the previous case, deep enough that stellar damping plays a role in the dynamics. These differences contribute to producing the different signatures of the nodding patterns for the two cases.

The transit timing variations described above and shown in Figure 8 exhibit many different modes of oscillation. In addition, this figure shows that it is plausible that the transit timing variations closely follow the time derivative of the resonance angle. When the resonance angle is nodding between the fixed points on either side of π , the derivative $\dot{\phi}$ decreases as ϕ passes π , and then increases before ϕ reaches the stable point opposite π and reverses direction. This type of motion qualitatively matches the transit timing variations calculated during the same period of time. When the resonance angle increases, the transit timing variations are positive; when the angle ϕ decreases, the TTVs are negative; and when

the angle passes through π , the angle slows down and the TTVs decrease. This complicated behavior is depicted by the 'double-peaked' patterns in Figure 8 between $t = 0 - 2$ years and $t = 20 - 25$ years.

The bottom panel in Figure 8 shows the Fourier Transforms (FT) of the TTV signal in 3 year windows which encapsulate times corresponding to the three different modes of libration exhibited by the resonance angle's nodding cycle. The three different power spectra in the bottom panel are color coded and correspond to the regions in the TTV signal highlighted with the same color. Accordingly, the dashed blue curve is the FT for the portion of the TTV signal in the middle panel that is highlighted in blue, near $t \sim 5 - 8$ years. During this window, the resonance angle librates around a single fixed point, and the peak frequency given by the FT is $f \sim 3 \text{ yr}^{-1}$. The red FT curve is from the TTV signal in the time window of $t \sim 10 - 13$ years, which corresponds to a dynamical state of the system which exhibits a net resonance angle circulation with aligned orbits. The peak frequency of the red FT curve is $f \sim 1.4 \text{ yr}^{-1}$. Finally, the green FT curve from the TTV signal between $t \sim 21 - 24$ years has a broad peak near frequencies $f \sim 0.5 - 0.8 \text{ yr}^{-1}$. Thus, for this particular system, observations of TTVs over a three year time interval can yield a range of fundamental frequencies that span a factor of ~ 4 ; the result depends on the three year window for which the transit times are observed.

Figure 9 shows the time evolution for a planetary system that is identical to that shown in Figure 8, except that the Hot Jupiter is taken to have smaller eccentricity $e_p = 0.01$. The behavior of the resonance angle is much the same as before, i.e., the transit timing variations calculated for the Hot Jupiter in this case contain all of the same qualitative features discussed in the previous example. For completeness, we have run additional scenarios where the mass of the smaller planet takes on different values. The resulting time evolution of the resonance angles (not shown) are, again, qualitatively similar. As the mass of the smaller body varies, however, the amplitude of the transit timing variations change in proportion, as outlined below (see also Agol et al. 2005; Veras et al. 2011).

Before leaving this section, we derive an approximate relation between TTV amplitudes (for the Hot Jupiter scenarios outlined above) and the time rate of change for the resonance angle $\dot{\phi}$. The applicable resonance angle for this situation is given in equation (2). The second time derivative for the resonance angle is given by

$$\begin{aligned} \ddot{\phi} &= (p + q)(\dot{n} + \ddot{\epsilon})_{\oplus} - p(\dot{n} + \ddot{\epsilon})_j - q\ddot{\omega}_{\oplus} \\ &\approx (p + q)\dot{n}_{\oplus} - p\dot{n}_j . \end{aligned} \tag{3}$$

Lagrange's planetary equations of motion provide us with the time rate of change for the

mean motion for both the Hot Jupiter and the Super Earth in this problem,

$$\dot{n}_\oplus = -\frac{3}{a_\oplus^2}(p+q)\partial_\phi\mathcal{R}_I, \quad (4)$$

$$\dot{n}_j = \frac{3}{a_j^2}p\partial_\phi\mathcal{R}_E, \quad (5)$$

where \mathcal{R}_I and \mathcal{R}_E are the disturbing functions for an internal and external perturber, respectively. Using a simple, time averaged form for the internal disturbing function,

$$\mathcal{R}_I = \frac{\mathcal{G}m_j}{a_j}[\alpha\mathcal{S} + \mathcal{F}_I e_\oplus \cos\phi], \quad (6)$$

and the external disturbing function,

$$\mathcal{R}_E = \frac{\mathcal{G}m_\oplus}{a_\oplus}[\mathcal{S} + \mathcal{F}_E e_\oplus \cos\phi], \quad (7)$$

where \mathcal{S} is the secular contribution to the disturbing function, we substitute these forms into equations (4) and (5) and get a relation between \dot{n}_\oplus and \dot{n}_j ,

$$\dot{n}_j = -\mu\frac{p}{p+q}\alpha^3\frac{\mathcal{F}_E}{\mathcal{F}_I}\dot{n}_\oplus, \quad (8)$$

where $\mu \equiv m_\oplus/m_j$ is the ratio of planet masses. In the case of a 2 : 1 resonance, $\alpha \approx 2^{-2/3}$, and the portion of equation (8) that depends on α simplifies to

$$\alpha^3\frac{\mathcal{F}_E}{\mathcal{F}_I} \simeq \alpha^3\frac{f_{31} - 2\alpha}{\alpha f_{31} - (2\alpha)^{-1}} = \alpha^2. \quad (9)$$

Substituting this simplification into equation (8) and combining the result with the approximate form for the second time derivative in equation (3), we find an expression relating the time rate of change for the Hot Jupiter’s orbital period to the second time derivative of the resonance angle,

$$\frac{\dot{T}}{T^2} \approx \frac{\mu}{2^3\pi\alpha^2}\ddot{\phi}, \quad (10)$$

where we have made use of the relation $\dot{n} = -2\pi T^2\dot{T}$ in this last line. Neglecting time variations in α , equation (10) can be directly integrated (over one orbit of the Hot Jupiter) to give us the desired relation between transit timing variations, ΔT , and the time derivative of the resonance angle, $\dot{\phi}$,

$$\Delta T \approx \frac{\mu T_j^2}{2^{5/3}\pi}\dot{\phi}. \quad (11)$$

To demonstrate the accuracy of equation (11), we take Figure 8 as an example. At peak TTV in Figure 8 (near the 5 year mark in the TTV panel of the figure), the resonance angle

is changing at a rate of $\approx 12 \text{ rad yr}^{-1} \sim 3.8 \times 10^{-7} \text{ rad sec}^{-1}$. The Hot Jupiter’s period is roughly 4 days ($\sim 3.5 \times 10^5 \text{ sec}$), and the outer planet has mass $m = 1 M_{\oplus}$ ($\mu \approx 0.003$). Substituting these quantities into the right hand side of equation (11) gives a timing variation $\Delta T \approx 14 \text{ sec}$, a result which is in good agreement with the figure. This result shows that the TTV signal can reveal intricate details about near-resonance nodding if such a system can be found in nature. The above derivation also confirms that the strength of the TTV signal increases with the mass of the exterior planet (Agol et al. 2005). We have run additional simulations with varying masses for the outer planet, up to $m = 10 M_{\oplus}$, and find that the amplitudes of the TTVs vary in proportion to the mass (as expected). In addition, equation (11) shows that the TTV signal increases as the square of the Hot Jupiter’s orbital period and one power of $\dot{\phi}$. Since $\dot{\phi}$ itself is inversely proportional to the period, the TTV amplitudes are directly proportional to the orbital period.

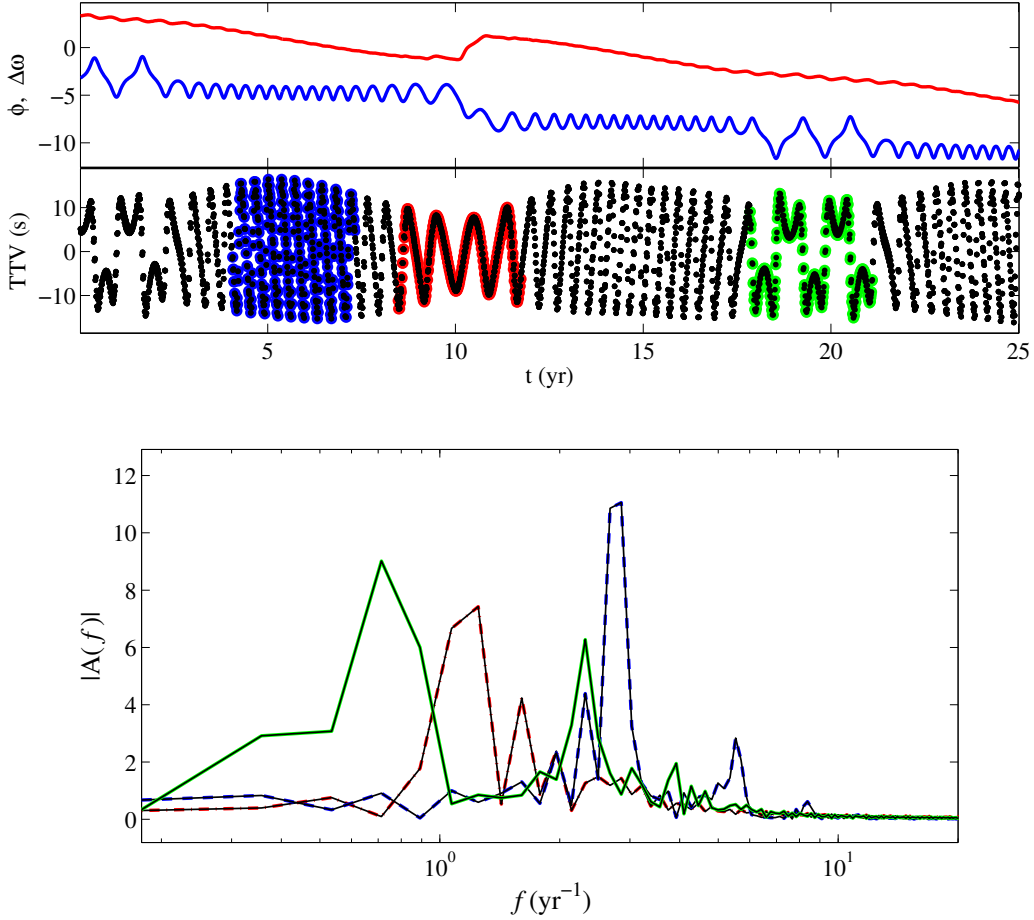


Fig. 8.— Results for a Hot Jupiter in a 4-day orbit, with eccentricity $e = 0.10$, and in an external 2:1 near-MMR with an Earth-mass planet ($m \approx 1M_{\oplus}$), both orbiting a $1M_{\odot}$ star. The *top panel* shows the time series for the resonance angle ϕ (blue curve) and the angle of apsides $\Delta\varpi$ (red curve) for the first 25 years (≈ 2000 Hot Jupiter orbits). The initial configuration of this system was chosen to obtain nodding behavior of the resonance angle. The *middle panel* shows transit timing variations (in seconds) for the Hot Jupiter during the simulation. Three separate 3-year windows highlight the TTV data (corresponding to different nodding modes of the resonance angle) in the colors (from left to right) blue, red, and green. Fourier Transforms for each highlighted portion are shown in the *bottom panel*, and are color coded to match their corresponding progenitive TTV signal. The bottom panel demonstrates that the fundamental frequency of the TTV signal for a system undergoing nodding motion can vary by a factor ~ 2 (either way) depending on resonance angle nodding effects.

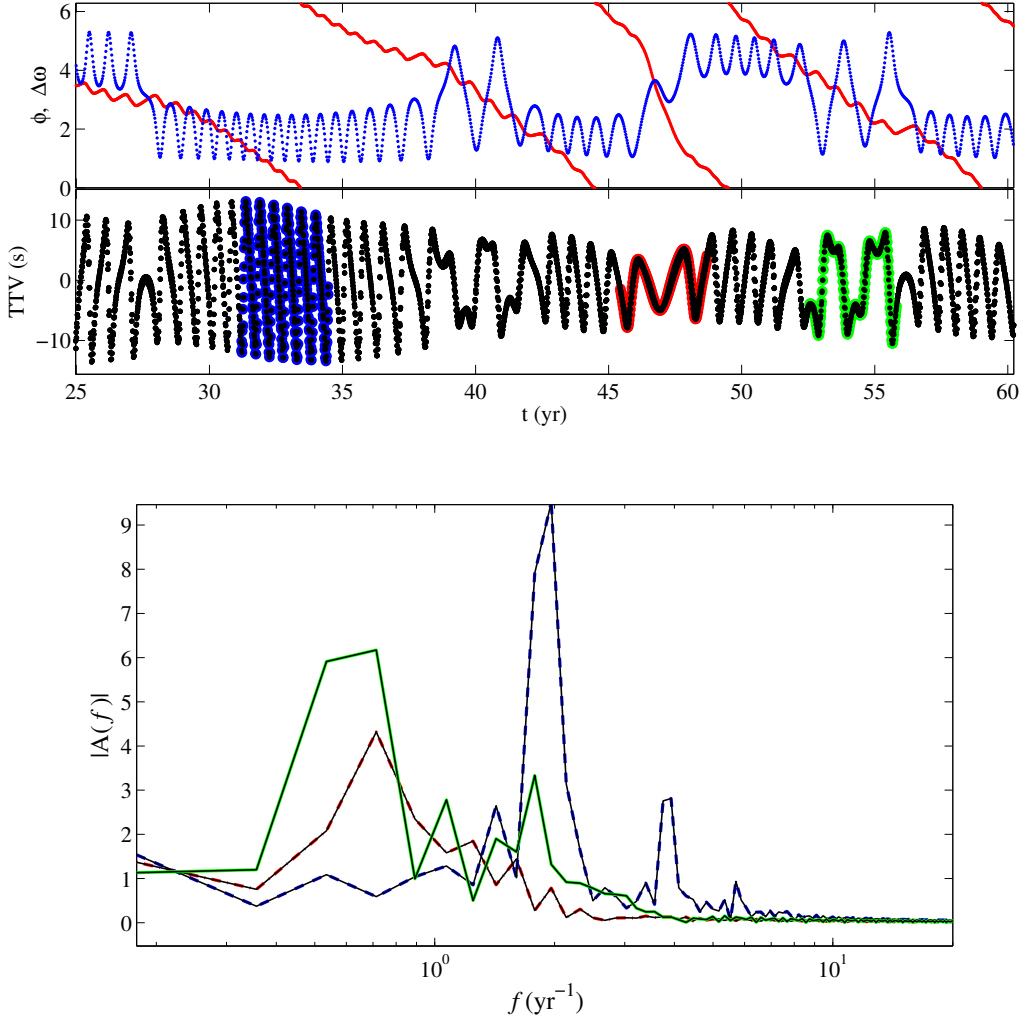


Fig. 9.— Results for a Hot Jupiter in a 4-day orbit, with eccentricity $e = 0.01$, and in an external 2:1 near-MMR with an Earth-mass planet ($m \approx 1M_{\oplus}$), both orbiting a $1M_{\odot}$ star. The *top panel* shows the time series for the resonance angle ϕ (blue curve) and the angle of apsides $\Delta\varpi$ (red curve) for ≈ 35 years (≈ 3000 Hot Jupiter orbits). The initial configuration of this system was chosen to obtain nodding behavior of the resonance angle. The *middle panel* shows transit timing variations (in seconds) for the Hot Jupiter during the simulation. Three separate 3-year windows highlight the TTV data (corresponding to different nodding modes of the resonance angle) in the colors (from left to right) blue, red, and green. Fourier Transforms for each highlighted portion are shown in the *bottom panel*, and are color coded to match their corresponding progenitive TTV signal. The bottom panel demonstrates that the fundamental frequency of the TTV signal for a system undergoing nodding motion can vary by a factor ~ 2 depending on resonance angle nodding effects.

3. Derivation of Model Equations for Nodding

In this section, we turn our attention to a Lagrangian formalism for the scenarios outlined in section 2. We analyze the equation of motion for the resonance angle in the restricted 3-body problem in order to identify the terms that encapsulate the dynamics of nodding. We choose a Lagrangian formulation instead of a Hamiltonian treatment purely for ease of physical interpretation. Consider three point masses that follow a hierarchical arrangement, $m_t \ll m_p \ll m_*$, where we denote orbital elements belonging to the test body with subscript t and those belonging to the planet with p . The three bodies are spatially separated so that m_t and m_p are gravitationally bound to m_* , but not bound to one another. Furthermore, suppose the orbits for m_t and m_p are coplanar, so they orbit m_* in the same plane. In what follows, first we provide a general treatment of the equations where we do not specify whether the planet’s orbit is interior or exterior to the test body’s orbit, but will later focus on the internal perturber case where $a_p < a_t$. The system sketched in the above outline is the planar restricted 3-body problem. This coming derivation follows a mathematical approach similar to that used in the text by Murray & Dermott (1999).

The argument angles (and hence the resonance angle), ϕ , for the disturbing function in the planar 3-body problem are given by a linear combination of the Eulerian angles

$$\phi = j_t \lambda_t + j_p \lambda_p + k_t \varpi_t + k_p \varpi_p, \quad (12)$$

where j_t , j_p , k_t , and k_p are integers, which sum to 0, $j_t + j_p + k_t + k_p = 0$. For such a system in resonance, $|j_p| : |j_t|$ is a ratio of small integers, and j_p and j_t are of opposite sign. From simulations, we found that the angle that tends to librate first is the angle corresponding to that of the circular restricted 3-body problem, i.e., where $k_p \equiv 0$ in the case where the perturbing planet’s orbit is strictly circular. This is because the strength functions associated with the resonance angle (besides those of the secular angles) are proportional to k_p factors of the planet’s orbital eccentricity e_p and k_t factors of the test body’s orbital eccentricity e_t . The perturbing planet and the primary mass (star) form a nearly Keplerian system. As a result, we assume that $\dot{\lambda}_p \approx n_p$ in this derivation. From this point forward, we note that orbital elements appearing without a subscript belong to the test body.

We find the first time derivative for the resonance angle

$$\dot{\phi} = j_t (n + \dot{\epsilon}) + j_p n_p - (j_p + j_t) \dot{\varpi}, \quad (13)$$

where the quantity

$$\dot{\epsilon} = \dot{\epsilon} + \dot{n} t \quad (14)$$

is introduced to avoid explicit time occurrences in the equation of motion (Brouwer & Clemence 1961) and where \dot{n} in equation (14) may originate from both damping effects

and the disturbing function. In the above derivation, it is important to note a few things. From this point forward we use the following notation; partial derivatives written as ∂_q operate only on explicit occurrences of the variable q , and otherwise vanish. Using a lowest eccentricity order form of Lagrange’s planetary equations of motion for $\dot{\underline{e}}$ and $\dot{\underline{\omega}}$, we can write

$$\dot{\underline{\omega}} = \frac{1}{na^2e} \partial_e \mathcal{R} , \quad (15)$$

and

$$\dot{\underline{e}} = -\frac{2}{na} \partial_a \mathcal{R} + \frac{e}{2na^2} \partial_e \mathcal{R} = \mathcal{S}_A \frac{2\alpha}{na^2} \partial_\alpha \mathcal{R} + \frac{e^2}{2} \dot{\underline{\omega}} , \quad (16)$$

where \mathcal{R} is the disturbing function (for either an interior or an exterior perturber), and where we introduce \mathcal{S}_A with $\mathcal{S}_A = \{1, -1\}$ for an internal or external perturber, respectively; this sign function arises from a change of variables from a_t to α , i.e., $a\partial_a = -\mathcal{S}_A\alpha\partial_\alpha$. We can rewrite equation (13) as

$$\dot{\phi} = (j_t + \mu\alpha^{\mathcal{S}_B} \mathcal{P}(\mathcal{R})) n + j_p n_p , \quad (17)$$

where $\mu = m_p/m_*$ is the mass ratio between the planet and the star, we introduce the quantity \mathcal{S}_B where $\mathcal{S}_B = \{0, 2\}$ for an internal or external perturber, respectively; we have also introduced the linear differential operator \mathcal{P} defined as

$$\mathcal{P} \equiv \Lambda^{-1}(h_\alpha \partial_\alpha - h_e \partial_e) . \quad (18)$$

In equation (18), $\Lambda \equiv \mathcal{G}m_p/a_p$ is the pre-factor to the disturbing function containing dimensional constants, and we introduce the quantities h_α , h_e , and β defined by

$$\begin{aligned} h_\alpha &\equiv 2j_t \mathcal{S}_A , \\ h_e &\equiv \frac{(j_t + j_p)\beta}{\alpha e} , \\ \text{and } \beta &\equiv 1 - \frac{j_t}{j_t + j_p} \frac{e^2}{2} . \end{aligned} \quad (19)$$

Note that when substituting Lagrange’s planetary equation of motion for $\dot{\underline{e}}$ in equation (16), we have kept contributions from variations to the disturbing function from α , whereas some treatments will ignore these contributions (e.g., MD99), equivalently asserting that $\partial_\alpha \simeq 0$. However, this contribution can be substantially larger (nearly 40 times greater) than the contribution to $\dot{\underline{e}}$ from the $\dot{\underline{\omega}}e^2/2$ term. The form in equation (17) makes it easier to take the second time derivative en route to the resonance angle’s equation of motion,

$$\ddot{\phi} = [j_t + \mu\alpha^{\mathcal{S}_B} \mathcal{P}(\mathcal{R})] \dot{n} + \mu n \alpha^{\mathcal{S}_B} \left[\mathcal{S}_B \frac{\dot{\alpha}}{\alpha} \mathcal{P}(\mathcal{R}) + \frac{d}{dt} \{ \mathcal{P}(\mathcal{R}) \} \right] . \quad (20)$$

Using the form of the operator \mathcal{P} given in equation (18), we can apply the chain rule for the time derivative in the last term of equation (20) to obtain

$$\frac{d}{dt} [\mathcal{P}(\mathcal{R})] = \dot{\mathcal{P}}(\mathcal{R}) + \mathcal{P}(\dot{\mathcal{R}}) . \quad (21)$$

The time derivative of the \mathcal{P} operator, for constant primary and secondary masses, and constant semi-major axis for the secondary mass, is given by

$$\dot{\mathcal{P}}(\mathcal{R}) = \Lambda^{-1} h_e \left[\frac{\beta^*}{\beta} \begin{pmatrix} \dot{e} \\ e \end{pmatrix} + \mathcal{S}_A \frac{2}{3} \begin{pmatrix} \dot{n} \\ n \end{pmatrix} \right] \partial_e \mathcal{R} , \quad \text{with } \beta^* \equiv 2 - \beta , \quad (22)$$

and

$$\mathcal{P}(\dot{\mathcal{R}}) = \dot{e} \mathcal{P}(\partial_e \mathcal{R}) + \mathcal{S}_A \frac{2}{3} \frac{\dot{n}}{n} \alpha \mathcal{P}(\partial_\alpha \mathcal{R}) + \dot{\varpi} \mathcal{P}(\partial_\varpi \mathcal{R}) + \dot{\phi} \mathcal{P}(\partial_\phi \mathcal{R}) . \quad (23)$$

Combining the previous two results with equation (20) gives

$$\begin{aligned} \ddot{\phi} = & \frac{\dot{n}}{n} \left[\dot{\phi} - j_p n_p + \mathcal{S}_A \frac{2}{3} \mu n \alpha^{S_B} \{ \mathcal{S}_B \mathcal{P}(\mathcal{R}) + \alpha \mathcal{P}(\partial_\alpha \mathcal{R}) + \Lambda^{-1} h_e \partial_e \mathcal{R} \} \right] \\ & + \mu n \alpha^{S_B} \left[\frac{\dot{e}}{e} \left(e \mathcal{P}(\partial_e \mathcal{R}) + \Lambda^{-1} h_e \frac{\beta^*}{\beta} \partial_e \mathcal{R} \right) + \dot{\phi} \mathcal{P}(\partial_\phi \mathcal{R}) + \dot{\varpi} \mathcal{P}(\partial_\varpi \mathcal{R}) \right] . \end{aligned} \quad (24)$$

Equation (24) is arranged so that disk damping effects can be easily included into the equation of motion – all time derivative operations of orbital elements have been collected and accounted for and occur as first order time derivatives. With this form, one can simply substitute Lagrange’s planetary equations of motion where necessary and remove all implicit instances of time from the equation of motion, i.e., all remaining operators act only as partial derivatives with respect to the orbital elements, independent of time. Along these lines, one could modify the time derivatives of the orbital elements to include external forces (e.g., damping)

$$\begin{aligned} \dot{n} &= (\dot{n})_{\text{dist}} + (\dot{n})_{\text{damp}} , \\ \dot{e} &= (\dot{e})_{\text{dist}} + (\dot{e})_{\text{damp}} , \end{aligned} \quad (25)$$

where $(\dot{q})_{\text{dist}}$ represent variations to the orbital element q due to the disturbing function, and $(\dot{q})_{\text{damp}}$ are variations caused by external forces due to interactions with, for instance, a circumstellar disk.

3.1. Specialization to the Case of External resonances

We will now focus an external $p + q : p$ resonance. For a given angle ϕ from equation (12), The simplest time averaged disturbing function (to second order in eccentricity) for an internal perturber takes the form

$$\mathcal{R}_\phi = \Lambda [\alpha (\mathcal{S}_1 + \mathcal{S}_2 \cos(\varpi - \varpi_p)) + \mathcal{R}_D \cos \phi] , \quad (26)$$

where

$$\begin{aligned}
\Lambda &\equiv \frac{\mathcal{G}m_p}{a_p}, \\
\mathcal{S}_1 &\equiv (e^2 + e_p^2) f_{s,1}(\alpha), \\
\mathcal{S}_2 &\equiv ee_p f_{s,2}(\alpha), \\
\mathcal{R}_D &\equiv e^q \mathcal{F}_1(\alpha) \quad \text{where} \quad \mathcal{F}_1(\alpha) \equiv (\alpha f_d(\alpha) + f_i(\alpha)),
\end{aligned} \tag{27}$$

(MD99). Under this scenario, the following quantities will have values $j_t = (p + q)$, $j_p = -p$, $\mathcal{S}_A = 1$, and $\mathcal{S}_B = 0$. Using the damping forms given above in equation (25), we rearrange equation (24) algebraically and use the time averaged form of the disturbing function in equation (26), and parse the equation of motion into generalized reoccurring operators, trigonometric functions of ϕ and $\Delta\varpi$, and damping terms. Note that, during this expansion, we expand the equation for \dot{e} to the second lowest order in eccentricity to retrieve a form that utilizes the parameter β . This procedure results in an equation of motion of the form

$$\begin{aligned}
\ddot{\phi} &= -\sin\phi \left[\mathcal{N}pn_p + (\mathcal{N} + \mu n \Lambda \mathcal{P}(\mathcal{R}_D))\dot{\phi} + \mathcal{J}(\alpha\mathcal{S}_1) + \mathcal{J}(\alpha\mathcal{S}_2) \cos(\Delta\varpi) + \mathcal{J}(\mathcal{R}_D) \cos\phi \right] \\
&\quad - \sin(\Delta\varpi) \left[\mu n \dot{\varpi} \Lambda \mathcal{P}(\alpha\mathcal{S}_2) + \mathcal{K}(\alpha\mathcal{S}_1) + \mathcal{K}(\alpha\mathcal{S}_2) \cos(\Delta\varpi) + \mathcal{K}(\mathcal{R}_D) \cos\phi \right] \\
&\quad + \left[\tilde{\mathcal{N}}(pn_p + \dot{\phi}) + \tilde{\mathcal{J}}(\alpha\mathcal{S}_1) + \tilde{\mathcal{J}}(\alpha\mathcal{S}_2) \cos(\Delta\varpi) + \tilde{\mathcal{J}}(\mathcal{R}_D) \cos\phi \right].
\end{aligned} \tag{28}$$

Here, new operators were introduced to compactify notation

$$\begin{aligned}
\mathcal{J}(\mathcal{Q}) &\equiv \mathcal{N}\mathcal{P}_n(\mathcal{Q}) + \mathcal{E}_\phi\mathcal{P}_e(\mathcal{Q}), \\
\mathcal{K}(\mathcal{Q}) &\equiv \mathcal{E}_\varpi\mathcal{P}_e(\mathcal{Q}), \\
\tilde{\mathcal{J}}(\mathcal{Q}) &\equiv \tilde{\mathcal{N}}\mathcal{P}_n(\mathcal{Q}) + \tilde{\mathcal{E}}\mathcal{P}_e(\mathcal{Q}),
\end{aligned} \tag{29}$$

with

$$\begin{aligned}
\mathcal{P}_n(\mathcal{Q}) &\equiv \frac{2}{3}\mu n [\alpha\Lambda\mathcal{P}(\partial_\alpha\mathcal{Q}) + h_e\partial_e\mathcal{Q}], \\
\mathcal{P}_e(\mathcal{Q}) &\equiv \mu n \left[e\Lambda\mathcal{P}(\partial_e\mathcal{Q}) + h_e\frac{\beta^*}{\beta}\partial_e\mathcal{Q} \right],
\end{aligned} \tag{30}$$

where \mathcal{Q} is some function of eccentricities and α given in equation (27),

$$\begin{aligned}
\mathcal{N} &\equiv -3\mathcal{C}(p + q)\mathcal{R}_D, \\
\mathcal{E}_\varpi &\equiv -\mathcal{C}\frac{\alpha}{e^2}\mathcal{S}_2, \\
\mathcal{E}_\phi &\equiv \mathcal{C}\frac{q\beta}{e^2}\mathcal{R}_D,
\end{aligned} \tag{31}$$

where $\mathcal{C} = \mu n/\alpha$, and finally

$$\tilde{\mathcal{N}} \equiv \left(\frac{\dot{n}}{n} \right)_{\text{damp}}, \quad \text{and} \quad \tilde{\mathcal{E}} \equiv \left(\frac{\dot{e}}{e} \right)_{\text{damp}}.$$

Each line of equation (28) can be analyzed to determine what contributions to the resonance angle's equation of motion come from the disturbing function's secular and direct portions (\mathcal{S}_1 , \mathcal{S}_2 , and \mathcal{R}_D from equation (26)) and what contributions might be expected to arise from external damping forces. The first line of equation (28) contains the immediate contributions from the direct part of the disturbing function – that is to say that each term inside the square brackets includes a factor of \mathcal{R}_D , but also included are higher order cross term contributions to the motion arising from secular effects on \mathcal{R}_D . The second line contains the contribution from the secular parts of the disturbing function – for the *circular* restricted three body problem, this line vanishes. The final line of equation (28) originates from the presence of damping forces like those introduced in equation (25).

We can expand each operator and determine to what order the eccentricity contributes to the overall magnitude in each individual term therein:

$$\mathcal{J}(\alpha\mathcal{Q}) = -\mathcal{C}^2\mathcal{R}_D \left[h_\alpha^2\partial_\alpha(\alpha^2\partial_\alpha\mathcal{Q}) - 2\alpha^2h_\alpha h_e\partial_e\partial_\alpha\mathcal{Q} + \alpha^2h_e^2\partial_e^2\mathcal{Q} - \left(\frac{q\beta^*}{e^2} + h_\alpha\right)\alpha h_e\partial_e\mathcal{Q} \right], \quad (32)$$

$$\mathcal{J}(\mathcal{Q}) = -\mathcal{C}^2\mathcal{R}_D \left[h_\alpha^2\alpha^2\partial_\alpha^2\mathcal{Q} - 2\alpha^2h_\alpha h_e\partial_e\partial_\alpha\mathcal{Q} + \alpha^2h_e^2\partial_e^2\mathcal{Q} - \left(\frac{q\beta^*}{e^2} - h_\alpha\right)\alpha h_e\partial_e\mathcal{Q} \right], \quad (33)$$

$$\mathcal{K}(\alpha\mathcal{Q}) = -\alpha\mathcal{C}^2e^{-1}\mathcal{S}_2 \left[\alpha^2h_\alpha\partial_e\partial_\alpha\mathcal{Q} - \alpha^2h_e\partial_e^2\mathcal{Q} + \left(\frac{q\beta^*}{e^2} + h_\alpha\right)\alpha\partial_e\mathcal{Q} \right], \quad (34)$$

$$\mathcal{K}(\mathcal{Q}) = -\mathcal{C}^2e^{-1}\mathcal{S}_2 \left[\alpha^2h_\alpha\partial_e\partial_\alpha\mathcal{Q} - \alpha^2h_e\partial_e^2\mathcal{Q} + \left(\frac{q\beta^*}{e^2} + 0\right)\alpha\partial_e\mathcal{Q} \right], \quad (35)$$

$$\tilde{\mathcal{J}}(\alpha\mathcal{Q}) = \frac{\mathcal{C}}{\alpha} \left[\frac{2}{3}\tilde{\mathcal{N}}h_\alpha\partial_\alpha(\alpha^2\partial_\alpha\mathcal{Q}) + \left(\tilde{\mathcal{E}}e\alpha h_\alpha - \frac{2}{3}\tilde{\mathcal{N}}\alpha^2h_e\right)\partial_e\partial_\alpha\mathcal{Q} - \tilde{\mathcal{E}}q\beta\partial_e^2\mathcal{Q} + \tilde{\mathcal{E}}\frac{q}{e}(6 - 5\beta)\partial_e\mathcal{Q} \right], \quad (36)$$

$$\tilde{\mathcal{J}}(\mathcal{Q}) = \mathcal{C} \left[\frac{2}{3}\tilde{\mathcal{N}}\alpha^2h_\alpha\partial_\alpha^2\mathcal{Q} + \left(\tilde{\mathcal{E}}e\alpha h_\alpha - \frac{2}{3}\tilde{\mathcal{N}}\alpha^2h_e\right)\partial_e\partial_\alpha\mathcal{Q} - \tilde{\mathcal{E}}q\beta\partial_e^2\mathcal{Q} + \alpha\left(\tilde{\mathcal{E}}q\beta^* + \frac{2}{3}\tilde{\mathcal{N}}h_e\right)\partial_e\mathcal{Q} \right]. \quad (37)$$

It is important to consider the magnitude of each of these operators to determine their significance in the equation of motion given in equation (28). Figures 10, 11, and 12 show the resulting magnitudes as a function of the test body eccentricity e for the terms between the square brackets in line 1, 2, and 3 of equation (28), respectively.

3.2. Analysis of the Expansion Terms

In this section we focus on the $\sin\phi$ part of equation (28) – the first line of the equation of motion for the resonance angle. As written in this compact form, there are only five

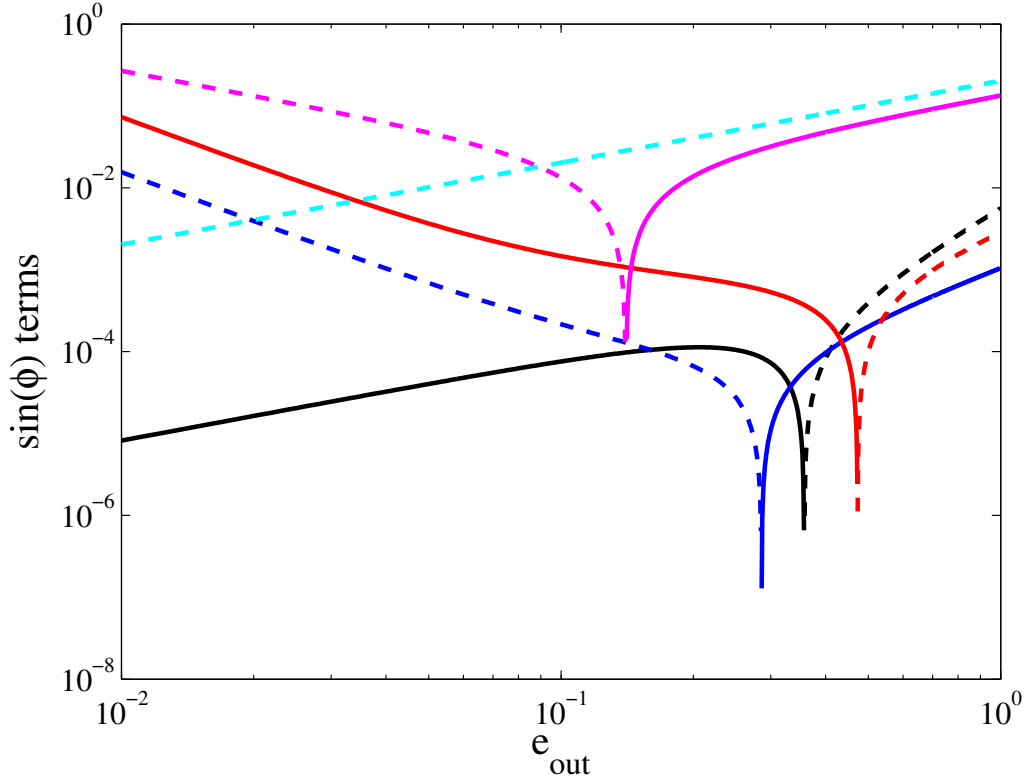


Fig. 10.— Magnitudes of coefficients for terms appearing in the first line ($\sin \phi$ part) of equation (28) as a function of test body eccentricity e . Solid curves represent positive values, and dashed curves negative. The magenta curve is the coefficient to $\dot{\phi}$ (second term in square brackets of line 1 of the equation). The cyan curve is the usual pendulum term (first term). The red curve is $\mathcal{J}(\mathcal{R}_D)$, the coefficient to $\cos \phi$ (last term). The blue curve is $\mathcal{J}(\alpha \mathcal{S}_2)$, the coefficient to $\cos(\Delta \varpi)$ (fourth term). The black curve is $\mathcal{J}(\alpha \mathcal{S}_1)$ (third term). The figure shows that, for low values of eccentricity, the pendulum term is not necessarily the dominant term. The figure depicts values for 2:1 external resonances, with $n = 2\pi$, $\mu = 10^{-3}$, and $e_p = 0.1$.

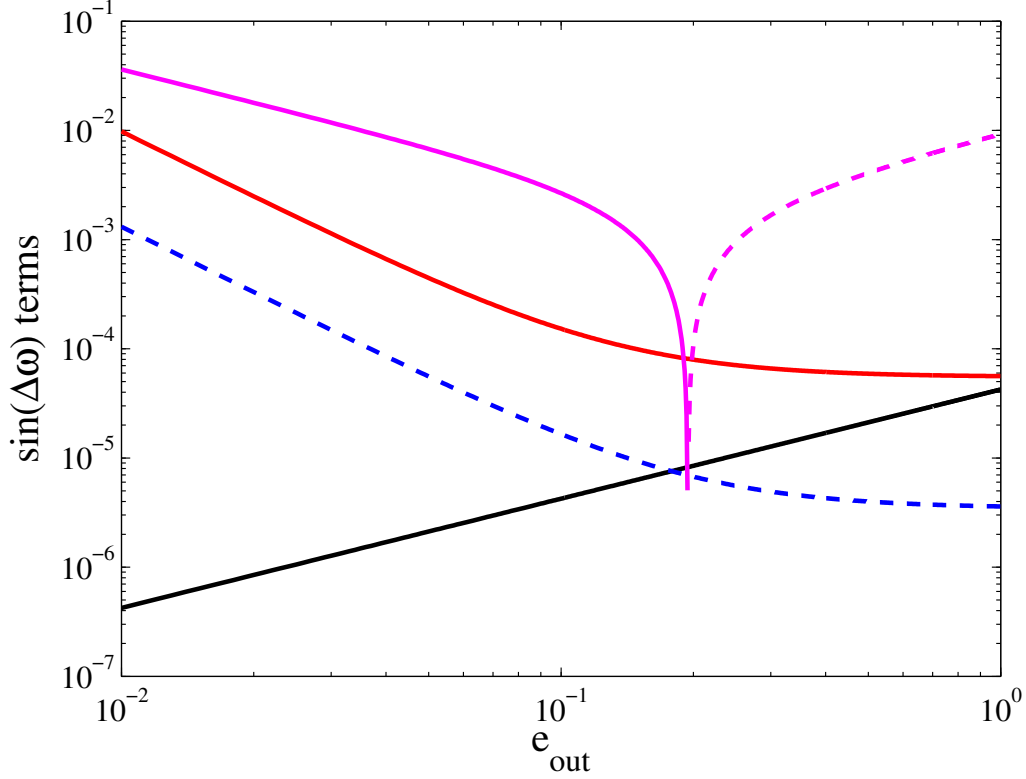


Fig. 11.— Magnitudes of coefficients for terms appearing in the second line ($\sin \Delta\varpi$ part) of equation (28) as a function of test body eccentricity e . Solid curves represents positive values, and dashed curves negative. The magenta curve is the coefficient to $\dot{\varpi}$ (first term in square brackets of line 2 of the equation). The red curve is $\mathcal{K}(\mathcal{R}_D)$, the coefficient to $\cos \phi$ (last term). The blue curve is $\mathcal{K}(\alpha\mathcal{S}_2)$, the coefficient to $\cos(\Delta\varpi)$ (third term). The black curve is $\mathcal{K}(\alpha\mathcal{S}_1)$ (second term). The only term independent of additional contributions from the angles (ϕ and $\Delta\varpi$) in this figure is the black curve. This figure depicts values for 2:1 external resonances, with $n = 2\pi$, $\mu = 10^{-3}$, and $e_p = 0.1$. The relative magnitudes are dependent on different factors of e_p . All strengths vanish for $e_p = 0$, i.e., for the case of the circular restricted 3-body problem.

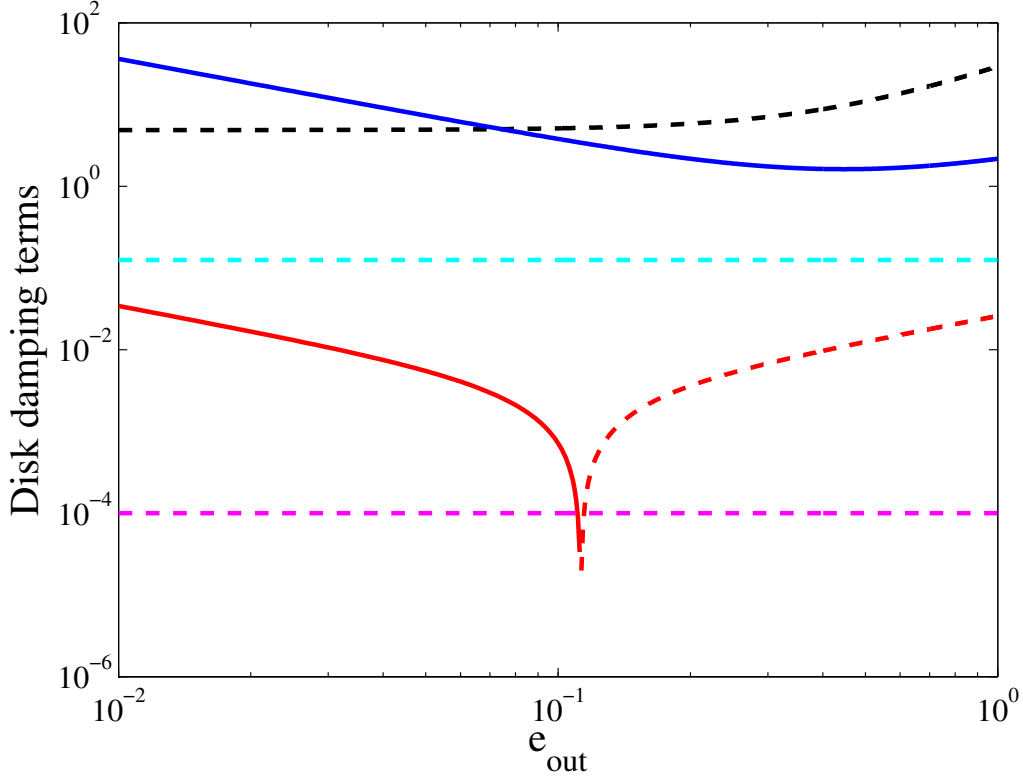


Fig. 12.— Magnitudes of coefficients for terms appearing in the damping terms (third line of the equation) of equation (28) as a function of test body eccentricity e , e.g., damping terms that may be considered as contributions to \dot{n} and \dot{e} (in addition to the usual Lagrange planetary equations) as in equation (25). Solid curves represent positive values, and dashed curves negative. The magenta curve is the coefficient to $\dot{\phi}$ (the first term). The red curve is $\tilde{\mathcal{J}}(\mathcal{R}_D)$, the coefficient to $\cos \phi$ (fourth term). The blue curve is $\tilde{\mathcal{J}}(\alpha \mathcal{S}_2)$, the coefficient to $\cos(\Delta \varpi)$ (third term) – it is not present in the circular restricted 3-body problem. The black curve is $\tilde{\mathcal{J}}(\alpha \mathcal{S}_1)$ (second term). The cyan curve is $\tilde{\mathcal{N}} p n_p$. This figure depicts values for 2:1 external resonances, with $n = 2\pi$, $\mu = 10^{-3}$, and $e_p = 0.1$. Damping parameters are $\tau_a = 10^4$ years and $\tau_e = 10^3$ years, where we have assumed a simple definition for damping parameters $\dot{a}/a = -\tau_a^{-1}$ and $\dot{e}/e = -\tau_e^{-1}$.

contributing terms contained within the square brackets. The first term, $\mathcal{N}pn_p \sin \phi$, when considered on its own, has been the focus of intense study in the circular restricted three body problem, and is called the pendulum model for obvious reasons. This model can be generalized by expanding each term within the square brackets via equations (31), (18), (27), (32), and (33) and keeping only the lowest eccentricity order contributions from each. Doing so gives the result

$$\ddot{\phi} \simeq -\sin \phi \left[-3/2h_\alpha \mathcal{C}(pn_p + \dot{\phi}) \mathcal{F}_1 e^q - q^2 \mathcal{C} \mathcal{F}_1 \dot{\phi} e^{q-2} + 2\mathcal{C}^2 q h_\alpha \mathcal{F}_1 (2\alpha \partial_\alpha f_{s,1} + f_{s,1}) e^q + \mathcal{C}^2 q^2 e_p f_{s,2} \mathcal{F}_1 \cos(\Delta\varpi) e^{q-3} - \mathcal{C}^2 q^3 (q-2) \mathcal{F}_1^2 \cos \phi e^{2(q-2)} \right]. \quad (38)$$

For non-circular perturber orbits, there is an additional contribution proportional to e_p^2 that has been excluded here, which may be significant given large enough values of e_p . Notice that, depending on the particular value of q , there are up to four different orders of eccentricity that show up, so we collect them in eccentricity order,

$$\ddot{\phi} \simeq -\sin \phi \left[\mathcal{C} \mathcal{F}_1 e^q \left\{ 2qh_\alpha \mathcal{C} (2\alpha \partial_\alpha f_{s,1} + f_{s,1}) - 3(p+q)pn_p - (3(p+q) + q^2 e^{-2}) \dot{\phi} \right\} + \mathcal{C}^2 q^2 e^{q-3} \mathcal{F}_1 \left\{ e_p f_{s,2} \cos(\Delta\varpi) - q(q-2)e^{q-1} \mathcal{F}_1 \cos \phi \right\} \right]. \quad (39)$$

However, the number of terms shown here can be further reduced. Although we are interested in a lowest eccentricity order study, we must also consider the lowest order terms in $\mathcal{C} \propto \mu$ as well. For a 2:1 period ratio, test body mean motion $n = 2\pi$, mass ratio $\mu \sim 10^{-3}$, and perturber eccentricity $e_p = 0.1$, Figure 10 depicts the corresponding relative strengths of each term contributing to the $\sin \phi$ part (first line) of equation (28).

For eccentricities $e \sim 0.1$, two terms in the expansion dominate. One term is the usual pendulum term, but the other term is something like a modified damping term (i.e., a term multiplying the time derivative $\dot{\phi}$). Although, $|\dot{\phi}|$ is generally less than unity for instances of libration, contributions from the $\dot{\phi}$ term can become quite large for sufficiently small eccentricities due to its e^{-1} dependence. In the figure, contributions from $\dot{\phi}$ and the pendulum term have the same sign (both curves are dashed lines, meaning less than zero on the log-log plot). To achieve nodding by way of the $\dot{\phi}$ term, one requires $\dot{\phi} < 0$ *in addition to* satisfying the constraint on the upper bound of the eccentricity, $e \leq 0.1$. The condition that $\dot{\phi} < 0$ for nodding to occur provides a simple explanation for the observation that the resonance angle tends to circulate on average over secular timescales in a preferred direction, usually resulting in a graph of ϕ versus t which is reminiscent of a stair case. The figure actually shows that this term is comparable to the pendulum term for all values of eccentricity, however it works to counteract the pendulum term for instances where $\dot{\phi} > 0$, and has opportunity to overwhelm the pendulum term only for $|\dot{\phi}| \gtrsim 2$.

Another term of significance appears in equation (39). For sufficiently small test body eccentricities, the term that is proportional to $e^{-2} \cos \phi$ plays an important role. As shown

in Figure 10, the $\cos \phi$ coefficient (red curve) surpasses the pendulum term (cyan curve) for eccentricities lower than ~ 0.03 . The greatest lower bound on eccentricity required for this term to take effect is

$$e \lesssim \left(\frac{\mu \mathcal{F}_1 \sqrt{\alpha}}{6} \right)^{1/3} .$$

When evaluated using the typical value $\mu = 10^{-3}$ in the external 2:1 case ($\mathcal{F}_1 \sim 0.27$), the above expression gives the restriction $e \lesssim 0.033$. Note that the $e^{-2} \cos \phi$ term is not present for those resonances with $q = 2$ (e.g., 3:1, 5:3, 7:5, etc...), and has opposite sign for resonances with $q = 3$ (e.g., 4:1, 5:2, 7:4, etc...) and above. However, for resonances of higher rank (higher q values), the eccentricity order increases relative to the order of the pendulum and the $\dot{\phi}$ terms, diminishing its importance.

Keeping only the two largest terms from Figure 10, the equation of motion can be reduced to the form

$$\ddot{\phi} \approx \mathcal{C} \mathcal{F}_1 \sin \phi \left[6n_p e + e^{-1} \dot{\phi} - \mathcal{C} \mathcal{F}_1 e^{-2} \cos \phi \right] . \quad (40)$$

This equation exhibits some of the nodding behaviors we see in the full problem (see section 2). The parameters and initial values must be fine-tuned for cases where eccentricities (and periastra) are independent of time (i.e., only special values allow for nodding). Under conditions where the eccentricity has time dependence, however, nodding is a robust phenomenon (it is much easier to find parameters for which nodding occurs). For the sake of simplicity, we adopt the parametric description for the time dependence of eccentricity

$$e(t) = e_0 - e_a \sin^2(\omega_e t) . \quad (41)$$

In many instances of nodding found from the numerical studies in section 2 but not featured in the figures, the test body’s orbital eccentricity evolves through large swooping double arches, spanning several orders of magnitude, reaching values as high as a few times 10^{-1} and as low as $10^{-2} - 10^{-3}$ (see top panel of Figure 6). This double arched pattern exhibited by the test particle’s orbital eccentricity is governed by the secular time scale, which typically falls in the range $\sim 10^2 - 10^3$ libration times, but can be much longer (e.g., Michtchenko et al. 2008b). The ansatz of equation (41) is used in order to model this behavior.

To demonstrate that this model exhibits some nodding behaviors, we integrate equation (40) using an adaptive fourth order Runge-Kutta integration scheme with $e = \text{constant}$ and with $e(t)$ given by equation (41). We note that this is a simple study in which the eccentricity evolution being used here is totally prescribed without feedback from the specific orbital parameters, so we do not expect the model to exhibit all of the intricate details exhibited by the full 3-body simulations presented in section 2. For the sake of definiteness, we take

$n \sim 1$, $\mathcal{C} \sim 10^{-2}$, and $\omega_e \sim 10^{-3} \text{ yr}^{-1}$ – the precise values of these parameters will depend on the orbital angles and mean motions, and the values we choose corresponds to orbital periods on the order of years, not days. Under the parametrically evolving eccentricity of equation (41), nodding is a robust phenomenon, even when considering the pendulum term alone. Guided by the pendulum model of the circular restricted 3-body problem, we take the initial conditions $(\phi, \dot{\phi}) = (\epsilon, 0)$, which places the system in a dynamically vulnerable position near a separatrix – any perturbations that supply additional action should eventually cause the pendulum to circulate rather than oscillate. Figure 13 demonstrates how a small amount of eccentricity variation can send such a system into bouts of nodding. However, the system need not be prepared in such a dynamically sensitive manner to see nodding. Figure 14 shows a system that would be stable in the absence of variable eccentricity, but where the inclusion of sufficient eccentricity cycling provides enough added action to induce nodding. In both Figures 13 and 14, we use $\mathcal{F}_I \simeq 0.27$, which is the approximate value obtained from equation (27) corresponding to a 2:1 period ratio with $\alpha \simeq 0.63$ (see MD99). Figure 15 shows the results when taking $\mathcal{F}_I = 1$ and using various combinations of the terms in equation (40) along with a time varying eccentricity as defined in (41). This figure demonstrates that the pendulum model alone is not enough to recover nodding behaviors, but nodding does appear in models that combine the pendulum term with either of the two additional terms in equation (40). Taken together, Figures 13 – 15 show that nodding behavior arises naturally in modified pendulum equations, such as those resulting from the expansion of the previous section.

It may be worth noting that another term in equation (39) is of order e^{-2} , which was ignored due to its contribution from e_p . However, this term could be of importance in cases where the test particle’s eccentricity is very low ($e \ll e_p$). Including this term leaves us with a form dependent upon $(\Delta\varpi)$,

$$\ddot{\phi} \approx \mathcal{C}\mathcal{F}_I \sin \phi \left[6n_p e + e^{-1} \dot{\phi} - \mathcal{C}\mathcal{F}_I e^{-2} \cos \phi - \mathcal{C}f_{s,2} e_p e^{-2} \cos(\Delta\varpi) \right]. \quad (42)$$

This equation will exhibit nodding, even for constant eccentricity (no time variation), as long as the eccentricity is sufficiently low and the periastron circulates on secular timescales.

We caution that this model certainly does not exhaust all possible terms that can lead to resonance angle nodding. In the regime where the perturbing planet’s eccentricity is non-negligible $e_p \gtrsim 0.1$, terms of first order in the planet’s eccentricity can become significant. In particular, the term in the disturbing function that goes like $\sim e_p \cos(\phi + (\Delta\varpi))$ can lead to some interesting modulations in the resonance angle, which ultimately may drive the resonance angle’s phase into the vicinity of a separatrix and induce nodding (K. Batygin, private communication).

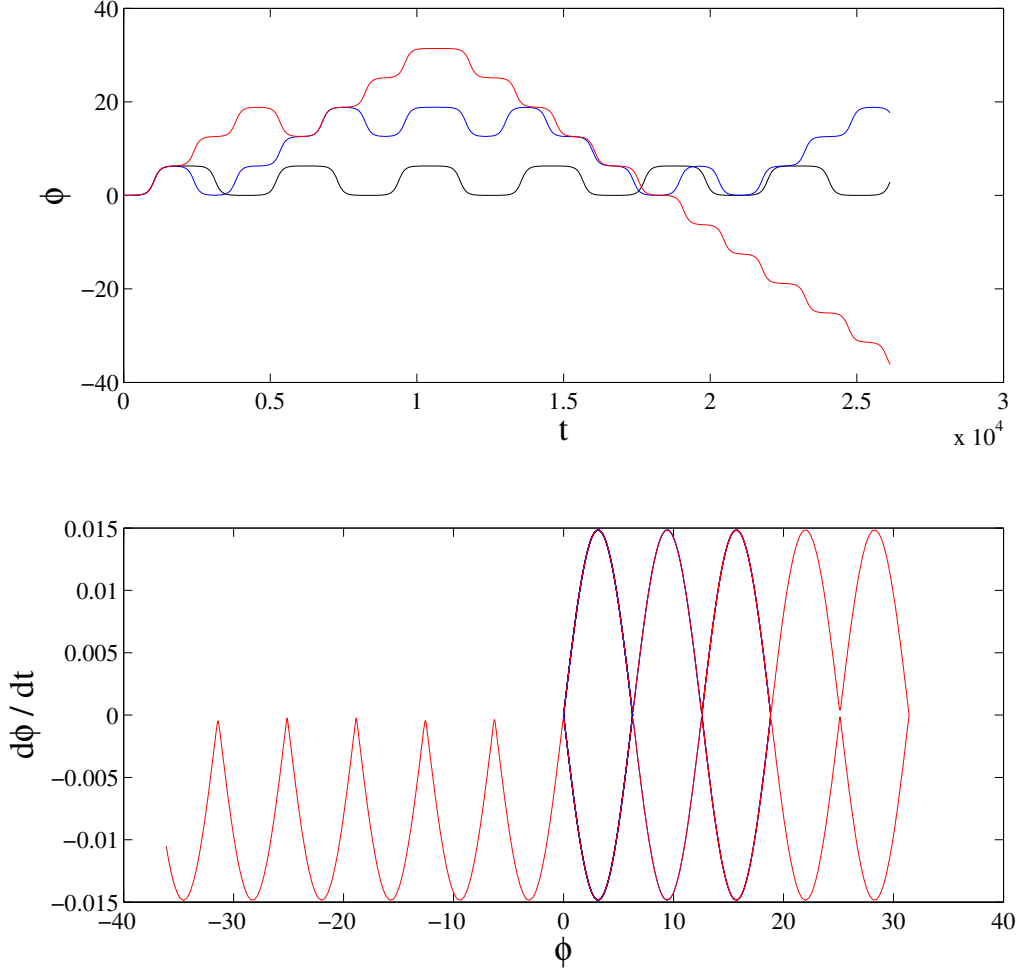


Fig. 13.— Solutions to the pendulum equation with constant eccentricity (black curve) and with eccentricity that varies by 0.1% on a secular timescale (blue and red curves). The system is set in a dynamically sensitive state near a separatrix with $\phi = 0.001$ and $\dot{\phi} = 0$ and integrated using 4th order Runge-Kutta scheme for 16 full secular cycles. The eccentricity is initially small ($e = 0.001$), and the pendulum term has no knowledge of the inner body’s eccentricity. The introduction of time varying eccentricity (even with small amplitude) induces circulation in the motion of the pendulum. The eccentricity cycle is phase shifted by π between the red and blue curves, where the blue curve begins at peak eccentricity. The bottom panel shows the phase trajectory for the resonance angle solutions in the top panel. The resonance angle is on phase trajectory that is very near a separatrix of the phase space. Note that in the phase diagram, the black curve is confined to $0 \lesssim \phi \lesssim 2\pi$, the blue curve is confined to $0 \lesssim \phi \lesssim 6\pi$, and the red curve is confined to $-12\pi \lesssim \phi \lesssim 10\pi$.

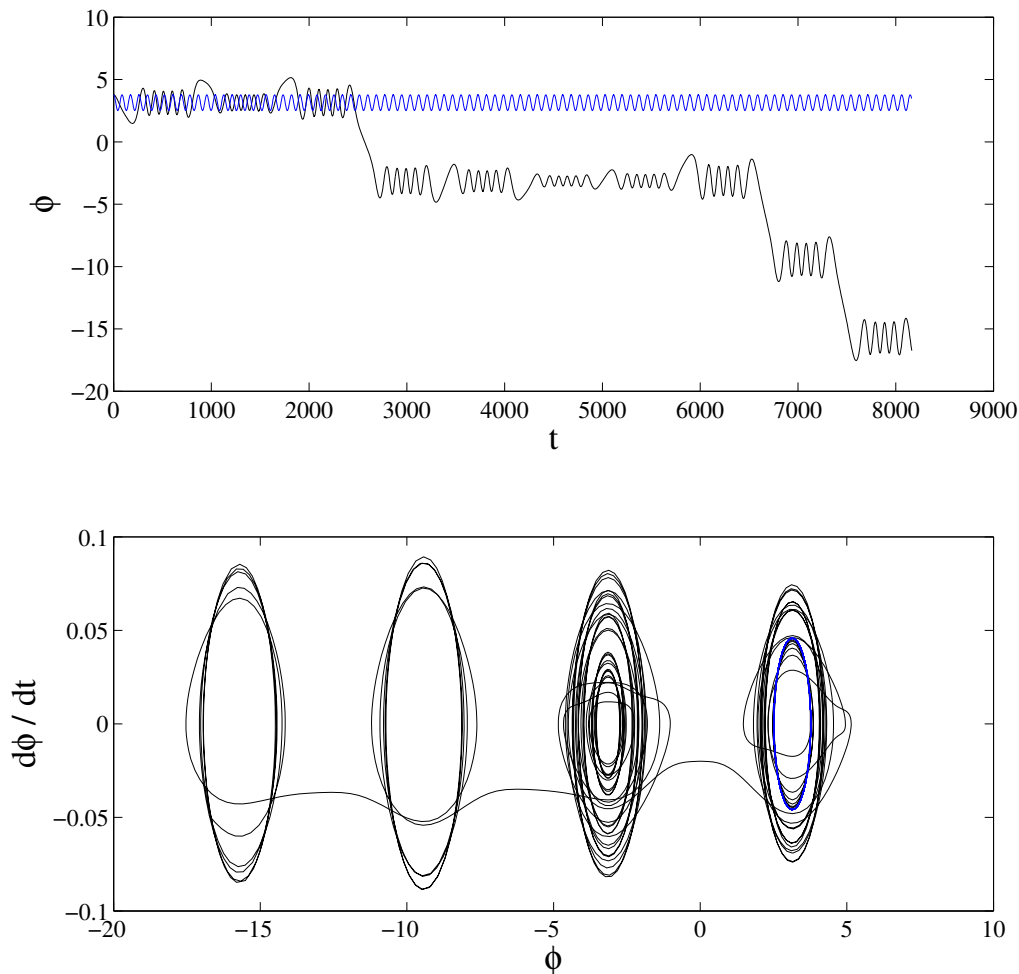


Fig. 14.— Solutions to the pendulum equation for initial values $e = 0.1$, $\phi = 1.2 \pi$, and $\dot{\phi} = 0$. Both solutions presented here are for the pendulum term with (i) constant eccentricity (blue curve) and (ii) with eccentricity that varies by 99% on a secular timescale (black curve). When eccentricity is constant, the system remains in an oscillatory state with amplitude $\Delta\phi \approx \pi/4$ around the point $\phi \simeq \pi$. For time varying eccentricity, the librations of the resonance angle become unbound before 2 complete secular cycles, and nodding ensues. The bottom panel shows the phase trajectory for the resonance angle solutions in the top panel. Oscillations of the resonance angle occur around points that are equivalently located at $\phi = \pi$ (modulo 2π).

The model developed in this section contains one important deficiency. The inner separatrix of the external resonance problem is completely missing from this model along with the unique characteristics distinguishing the external resonance from the internal one. This separatrix originates because of a bifurcation that occurs for the external resonance when $e \sim 0.1$, and is responsible for asymmetric resonances that have been observed in simulations for that regime (e.g., Callegari et al. 2004, Lee 2004). As a result, $\phi = \pi$ (or a point nearby) becomes a hyperbolic fixed point. Given that the test body’s eccentricity must be sufficiently large before this bifurcation occurs may suggest that more terms of the disturbing function are required in the time averaged treatment to recover these dynamics. More work must be done in order to elucidate this issue.

4. Conclusion

This paper presents an investigation of nodding behavior for planetary systems that are near mean motion resonance, with a focus on resonance angles corresponding to the 2:1 MMR. For systems that experience the nodding phenomenon, the resonance angle librates (oscillates) for several cycles, then circulates for one or more cycles, and then resumes its oscillatory motion (libration). The process repeats, so that even though the resonance angle is primarily in oscillation, the phase of the resonance angle nonetheless accumulates over time. In the extreme version of this behavior, the resonance angle can oscillate for one cycle, circulate for the next cycle, and then repeat the process; the resonance angle moves continually back and forth between the two types of motion, so that the resonance angle has an effective period of oscillation that is ~ 2 times longer than the usual period for MMR (see Figures 3, 8, and 9). Our numerical exploration of Section 2 shows that the nodding phenomenon arises in a wide variety of planetary systems (see Figures 1 – 9).

Nodding can be described as complex motion near a separatrix in the phase space of the resonance angle. Both internal and external resonances can exhibit nodding, but there exist prominent qualitative differences in the nodding signatures between the two configurations. The phase space for internal resonances contain one separatrix, whereas the phase space for external resonances can contain two distinct separatrices. The qualitative differences are mainly due to the existence of asymmetric external resonances, which arise when the orbital eccentricity for the outer (smaller) body becomes sufficiently large. Circulation of the resonance angle over secular times is common when the planet’s orbital eccentricity is sufficiently large, i.e., $e_p \gtrsim 0.02$. Nonetheless, the essential ingredients for nodding behavior are the presence of a separatrix and a means to cross it. Note that separatrix crossing can occur in sufficiently complex systems (e.g., the driven, inverted pendulum; Acheson 1995)

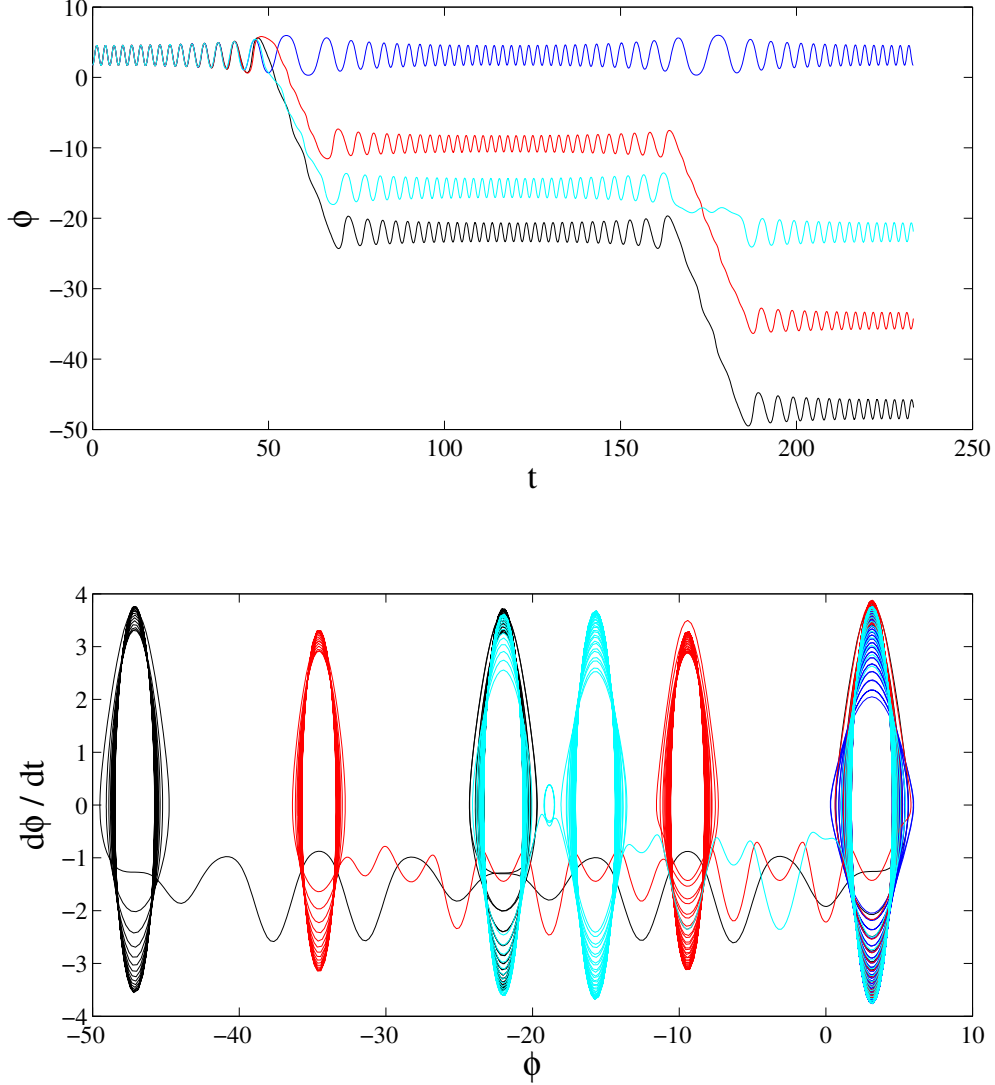


Fig. 15.— The result of numerically integrating equation (40) using parameters $T_{orb} = 100$ days, $T_{sec} = T_{orb} \times 10^{2.94}$, $\mu = 10^{-3}$, $e_0 = 0.32$, $e_a = 0.28$, $\mathcal{F}_1 = 1$, and the orbiting bodies in a perfect 2:1 orbital period ratio. The blue curve shows the solution for the pendulum term alone; the black curve shows the solution for the pendulum term plus the term that goes like $\dot{\phi}$; the cyan curve includes the pendulum term and the $e^{-2} \cos \phi$ term; the red curve shows the solution when including all terms in equation (40). The only model out of the four depicted here that doesn't exhibit nodding is that consisting of the pendulum term in isolation. Inclusion of the two terms of lower eccentricity order and in any combination results in nodding. The timescale depicted in the top panel is in years. The bottom panel shows the phase trajectory for the resonance angle solutions in the top panel.

and can arise due to chaos (e.g., Morbidelli & Moons 1993).

Exoplanets that transit their host stars are expected to exhibit transit timing variations when additional perturbing bodies are present, and the variations are greatest when the perturbing body is either in or near mean motion resonance with the transiting body. For systems where the perturbing body is near MMR, there is a possibility that the resonance angle may undergo nodding. In such systems, both the amplitude and the period of the TTVs depend on the window of time over which the system is observed (see Figures 8 and 9). If the observations are made over a time interval where the resonance angle of the system oscillates for many cycles, the TTVs have their usual interpretation. In the limit where the resonance angle goes back and forth between oscillating and circulating every cycle, the effective frequency of the TTVs is lower (than in the purely oscillatory case) by a factor of ~ 2 . Nodding behavior that is intermediate between these two cases is also possible, and produces TTVs with intermediate frequencies (see the power spectra in the bottom panels of Figures 8 and 9). Note that the amplitudes of the TTVs vary with the mode of nodding/oscillation (for the same masses). The added complexity in the dynamics due to nodding can thus introduce corresponding difficulties in interpreting the source of transit timing variations. This possible complexity should be kept in mind when searching for hidden exoplanets through measurements of transit times.

Using Lagrange’s planetary equations of motion, we have derived a set of generalized equations of motion for the resonance angle by including additional terms in the expansion in order to account for nodding behavior (see Section 3). This derivation uses the time-averaged disturbing function and initially keeps terms up to second order in eccentricity. As expected, the initial expansion includes a large number of terms. We then performed an analysis that uses results from the full numerical treatment to determine the relative sizes of the various terms in the expansion over the parameter space of interest (see Figures 10, 11, and 12). For some parameter values, we found that some of the “higher order” terms (those left out of the MD99 derivation) can dominate over those terms commonly used in deriving the pendulum model, which provides a standard description for MMR.

Given the expected magnitudes of the expansion terms, we have constructed a modified model for MMR, where the equation of motion includes two additional terms and thus allows for more complex dynamics (see equation [40]). This equation exhibits the nodding behavior found for interior resonances of the full problem. However, nodding only occurs for particular values of the eccentricity and argument of periastron, where both variables are considered as constants. We then generalized this model one step further by allowing the eccentricity to change with time (see equation [41]), motivated by the secular cycles of eccentricity variation often seen in two planet systems (including the orbits of Jupiter and Saturn in our

solar system – see MD99). With this generalization to include eccentricity cycles, nodding is a robust phenomenon and occurs for a wide range of the other parameters. Even when considering the pendulum term in isolation, the cycling of eccentricity on secular timescales can provide sufficient perturbations to induce nodding behaviors in certain dynamically vulnerable configurations.

The model from section 3 contains at least one deficiency. The inner separatrix of the external resonance problem is missing from the model, along with the unique characteristics distinguishing the external resonance from the internal one. This additional separatrix originates for the external resonance for larger outer body eccentricities, when $e \sim 0.1$, and is reminiscent of the pitchfork bifurcation shown in Figure 7. This separatrix is responsible for the asymmetric resonances that have been observed for that regime. As a result, some region in the neighborhood of $\phi = \pi$ contains a hyperbolic fixed point. Given that the eccentricity of the test body must be significantly large before this bifurcation occurs, additional terms in the expansion of the disturbing function may be required to recover these dynamics. This issue is left for future work.

The results of this work, and the existence of nodding phenomena in general, have two principal implications: [1] Planetary systems near MMR display complex and sometimes unexpected behavior, so that nodding poses a rich set of dynamical questions for further work. It would be interesting to determine the minimal requirements for a dynamical system to exhibit nodding, and to explore the relationship between nodding and chaotic motion. [2] The main application of this work to observations lies in the interpretation of transit timing variations. If an observed system with TTVs experiences nodding, then the inferred mass and orbital elements of the unseen perturbing body could vary, depending on the time interval of observation (Figures 8 and 9). A more complete exploration of parameter space, with a focus on the TTV signals (analogous to Veras et al. 2011), should be undertaken in the future.

This paper benefited from discussions with many colleagues, especially Konstantin Batygin, Philip Holmes, Greg Laughlin, Man Hoi Lee, and Matthew Payne. We also thank an anonymous referee for useful comments that improved the manuscript. This work was supported by NSF grant DMS-0806756 from the Division of Applied Mathematics, a Rackham Predoctoral Fellowship from the University of Michigan (JAK), NASA grant NNX11AK87G (FCA), and NSF grants DMS-0907949 and DMS-1207693 (AMB).

REFERENCES

- Acheson, D.J. 1995, Proc R Soc Lond, A 448, 89, 95
- Adams, F. C., & Laughlin, G. 2006, ApJ, 649, 992
- Adams, F. C., Laughlin, G., & Bloch, A. M. 2008, ApJ, 683, 1117
- Agol, E., Steffen, J., Sari, R., & Clarkson, W. 2005, MNRAS, 359, 567
- Batygin, K., & Morbidelli, A. 2011, Celest. Mech., 111, 219
- Batygin, K., & Morbidelli, A. 2012, AJ, submitted
- Beauge, C. 1994, Celest. Mech., 60, 225
- Beauge, C., & Michtchenko, T. A. 2003, MNRAS, 341, 760
- Bodenheimer, P., Laughlin, G., & Lin, D.N.C. 2003, ApJ, 592, 555
- Brouwer, D., & Clemence, G.M. 1961, Methods of Celestial Mechanics (Academic Press)
- Callegari Jr., N., Michtchenko, T., & Ferraz-Mello, S. 2004, Celest. Mech., 89, 201
- Cochran, W. D., Fabrycky, D. C., & Torres, G. et al. 2011, ApJS, 197, 7
- Exoplanets Data Explorer, September 2012, <http://exoplanets.org/>
- Fabrycky, D. C., Lissauer, J. J., & Ragozzine, D., et al. 2012, arXiv:1202.6328v2
- Ferraz-Mello, S. 1988, AJ, 96, 400
- Ferraz-Mello, S., Beauge, C., & Michtchenko, T. 2003, Celest. Mech., 87, 99
- Greenberg, R., & Franklin, F. 1975, MNRAS, 173, 1
- Goldreich, P., & Soter, S., 1963, Icarus, 5, 375
- Guckenheimer, J., & Holmes, P. 1983, Nonlinear Oscillations, Dynamical Systems, and Bifurcations of Vector Fields (Springer-Verlag New York)
- Henrard, J., Lemaître, A., Milani, A., & Murray, C. D. 1986, Celest. Mech., 38, 175
- Holman, M. J., Fabrycky, D. C., Ragozzine, D. et al. 2010, Science, 330, 51
- Hut, P. 1981, A&A, 99, 126

- Ketchum, J. A., Adams, F. C., & Bloch, A. M. 2011a, *ApJ*, 726, 53
- Ketchum, J. A., Adams, F. C., & Bloch, A. M. 2011b, *ApJ*, 741, L2
- Kley, W., Lee, M. H., Murray, N., & Peale, S. J. 2005, *A&A*, 437, 727
- Lecoanet, D., Adams, F. C., & Bloch, A. M. 2009, *ApJ*, 692, 659
- Lee, M.-H., & Peale, S. J. 2002, *ApJ*, 567, 596
- Lee, M.-H., 2004, *ApJ*, 611, 517
- Michtchenko, T., Beauge, C., & Ferraz-Mello, S. 2008a, *MNRAS*, 387, 747
- Michtchenko, T., Beauge, C., & Ferraz-Mello, S. 2008b, *MNRAS*, 391, 215
- Morbidelli, A., & Moons, M. 1993, *Icarus*, 102, 316
- Murray, C. D., & Dermott, S. F. 1999, *Solar System Dynamics* (Cambridge: Cambridge Univ. Press) (MD99)
- Nesvorný, D., & Morbidelli, A. 2008, *Icarus*, 688, 636
- Quillen, A. C. 2006, *MNRAS*, 365, 1367
- Rein, H., & Papaloizou, J.C.P. 2009, *A&A*, 497, 595
- Snellgrove, M. D., Papaloizou, J.C.B., Nelson, R. P. 2001, *A&A*, 374, 1029
- Veras, D., Ford, E. B., & Payne, M. J. 2011, *ApJ*, 727, 74